Production of ϕ Mesons as a Function of Multiplicity & Spherocity

Master's Thesis

Adrian Fereydon Nassirpour
Supervised by Peter Christiansen

Lund University
Division of Particle Physics
Department of Physics

July 16, 2017

LUNDS UNIVERSITET

Abstract

The purpose of this project is to further investigate whether the collective behavior observed in high energy proton-proton (p-p) collision can be attributed to the formation of Quark-Gluon Plasma (QGP). This is done by measuring the production rate of the strange ϕ meson in high multiplicity p-p collisions at $\sqrt{s_{\mathrm{NN}}} = 13$ TeV. The high multiplicity p-p events are then divided into different transverse spherocity bins, in order to gauge whether the ϕ production is dominated by events that are geometrically characterized as jet-like or isotropic. The results, although leaving some questions to be asked regarding the simulated detector efficiency, present a pronounced enhancement of ϕ mesons in high multiplicity collisions, and further state that the strangeness enhancement is dominated by events with an overall isotropic shape. These findings suggest that Lund string-like models might be inadequate at fully describing high multiplicity p-p collisions. It also gives further support to the idea that the preferred mechanism of ϕ particle production might follow a statistical, hydrodynamical model, through the formation of a QGP phase.

Acknowledgments

I would like to thank my supervisor, Peter Christansen, not only for his support and guidance, but also for giving me the opportunity to undertake this exciting project. I would also like to thank the remaining ALICE staff at Lund University, David Silvermyr, Anders Oskarsson, Evert Stenlund, Martin Ljunggren, Jonatan Adolfsson and Vytautas Vislavičius for help with coding and proofreading throughout my project.

Lastly, I'd like to thank the bachelor and master's students that I've shared office with throughout the year; Adam Benny Johansson, Rickard Lydahl, Maria Mårtensson, Madeleine Sjögren, Madeleine Burheim and Anna Onnerstad for help with coding and proofreading, as well as creating a good mood in the office.

Populärvetenskaplig Sammanfattning

Under detta projekt så analyserades högenergetiska proton-proton kollisioner i syftet för att bättre förstå hur den starka växelverkan med hjälp av gluoner håller ihop kvarkar, en av materians fundamentalpartiklar, för att bilda hadroner. Dessa högenergetiska protoner accelereras upp till 99 % av ljusets hastighet med hjälp av partikelacceleratorn "Large Hadron Collider" (LHC), innan de till slut kolliderar mot varandra i speciellt kontruerade partikeldeteckorer. Kollisionerna är tillräckligt kraftfulla för att kvarkarna momentant frigörs från sina hadroner, vilket gör det möjligt att studera hur gluonerna och kvarkarna interagerar med varandra.

Om kollisionen är tillräckligt kraftfull så kan en Kvark-Gluon Plasma bildas. Kvark-gluon plasman är ett väldigt kompakt och varmt materietillstånd som förhåller sig i termiskt och kemiskt ekvilibrium. I en kvark-gluon plasma så är kvarkarna och gluonerna inte bunda innuti hadroner, utan istället beter sig som en kollektiv, perfekt (nästintill ingen viskositet) vätska. Plasman bildas bara under en väldigt kort tidstund innan det kyls ner. Efter nedkylningen så är kvarkarna återigen bunda inom individuella hadroner. Att kontinuerligt hålla kvark-gluon plasman vid korrekt tryck och temperatur skulle kräva enorma resurser, vilket gör det praktiskt omöjligt att direkt verifiera om plasman har bildats. Istället så undersöks hur andra producerade partiklar interagerar med kvark-gluon plasman, för att bättre förstå hur den fungerar. Tecken på att kvark-gluon plasma har bildats brukar vara att partiklarna i kollisionen har ett kollektivt beteende, en ökad produktion av vissa parikelsorter och andra fenomen.

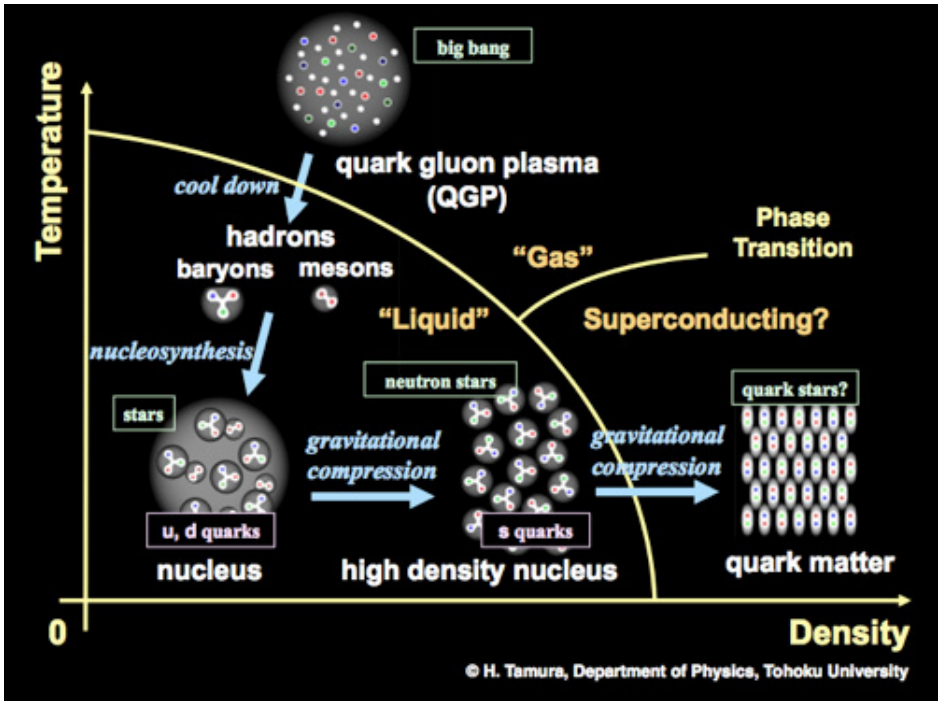

Figure 1: En bild som visar hur kvark-glon plasman, och olika fastransitoner förhåller sig till tryck och temperatur [1].

Ett problem uppstod dock när man märkte att några av de fenomen som ansågs vara signaturer av kvark-gluon plasman även hittades i kollisioner som man *inte* trodde var energetiska nog för att kunna bilda kvar-gluon plasma. Därefter ifrågasattes idén om huruvida kvark-gluon plasma faktiskt någonsin bildats i en kontrollerad partikelkollision. Huvudsyftet med detta projekt är att undersöka hur produktionen av ϕ mesonen, en partikel som tros har en ökad produktionshalt i en eventuell kvark-gluon plasma, beter sig för varierande proton-proton kollisioner av olika energigrader.

List of Acronyms

- ALICE : A Large Ion Collider Experiment
- ATLAS : A Toroidal LHC Apparatus
- BW : Briet-Wigner
- CERN : European Organization of Nuclear Research
- CMS : Compact Muon Solenoid
- HEP : High Energy Physics
- ITS : Inner Tracking System
- LHC : Large Hadron Collider
- LSME : Like-Sign Mixed-Event
- LSSE : Like-Sign Same-Event
- MC : Monte Carlo
- MRPC : Multigap Resistive Plate Chambers
- MWPC : Multi-Wire Proportional Chamber
- p-p collisions : proton-proton collisions
- PID : Particle Identification
- PMT : Photon-Multiplier Tube
- QCD : Quantum Chromodynamics
- QED : Quantum Electrodynamics
- QGP : Quark Gluon Plasma
- TOF : Time-Of-Flight
- TPC : Time Projection Chamber
- USME : Unlike-Sign Mixed-Event
- USSE : Unlike-Sign Same-Event

Contents

1 Introduction

The idea of observing free, or deconfined, quarks and gluons has been around since the creation of the framework describing the strong interaction, Quantum Chromo Dynamics (QCD). The deconfinement of quarks is studied through the formation of what is known as the Quark-Gluon Plasma (QGP). The QGP, a 'soup' of gluons and quarks, can only form through large energy densities, either by deconfining the quarks due to thermal excitations, or by compressing them together. As of now, it is not possible to study the QGP at macroscopic levels, due to the enormous resources it would require to attain the necessary energy density. This is not necessarily the case on the microscopic scale, where the required conditions for the QGP can be created by accelerating and colliding heavy ions, near the speed of light. Although the QGP would quickly cool down and produce ordinary hadrons, it is possible to find signs of the QGP by studying collective behavior, how the particles interact with the QGP, and other auxiliary effects.

However, developments from a CMS study performed in 2010 has found that some of the collective behavior found in heavy ion collisions, that are used in order to justify the creation of QGP, also appear in proton-proton (p-p) collisions (collisions that are not theoretically viable to create QGP) [2]. A point of contention was thus created, regarding the question of whether man-made QGP has ever been created. The main purpose of this analysis is to contribute to this discussion, to see whether p-p collisions can evolve towards a QGP-phase or not. The analysis is performed by studying p-p collisions with a center of mass energy of $\sqrt{s_{NN}} = 13$ TeV, gathered from A Large Ion Collider Experiment (ALICE), at the European Organization for Nuclear Research (CERN). A study from ALICE recently showed that there is an enhancement of various strange particles produced in high energy p-p collisions. This analysis will be undertaken in a similar vein, by studying the amount of ϕ mesons (a meson consisting of an $s\bar{s}$ pair) produced, versus different geometric constraints of the p-p collisions.

2 Theory

2.1 The Standard Model

The Standard Model (SM) is a theoretical framework that attempts to describe all the phenomena of particle physics, by unifying the fundamental forces at a sub-atomic level [3]. The four fundamental forces are as follows:

- The electromagnetic interaction (described through the framework of Quantum Electro Dynamics, QED).
- The weak interaction (described together with the electromagnetic interaction in the electroweak unification).
- The strong interaction (described through the framework of Quantum Chromodynamics, QCD).
- Gravity, which is expected to be negligible on the sub-atomic level, and will as such not be discussed further.

The SM can be seen in Fig. 2, and consists of elementary particles divided into two different classes: *fermions* and *bosons*. The fermions are considered the 'building-blocks' of matter, and come in 24 different variants (12 particles + 12 anti-particles). The fermions all consist of spin 1/2 particles, and thus all obey the Pauli-exclusion principle. The fermions are further divided into two separate classes, the *quarks* (that together build hadrons, such as the proton, which will be covered more thoroughly in Section 2.2) and *leptons* (such as the electron). Each quark and lepton has their own unique mass, and are all electrically charged (discounting the neutrinos). The fermions all have an anti-particle partner, with the exact same mass, but opposite quantum numbers (such as the electrical charge, lepton numbers etc). The quarks and leptons are further divided in one of three different generations. As can be seen in Fig. 2, the average mass of the fermions increase with each generation.

In contrast to the fermions, the bosons are all spin-1 or spin-0 particles, and thus are not bound by the Pauli-exclusion principle. There are currently five different known bosons within the SM; four gauge bosons (spin-1), and one scalar boson (spin-0) [5]. The gauge bosons act as mediator particles for the three aforementioned fundamental forces, and interact with the different fermions according to their charges. The photon (γ) mediates the electromagnetic force, the gluon (g) mediates the strong force, and the $W^{\pm}$ boson, together with the Z^0 boson, mediates the weak force.

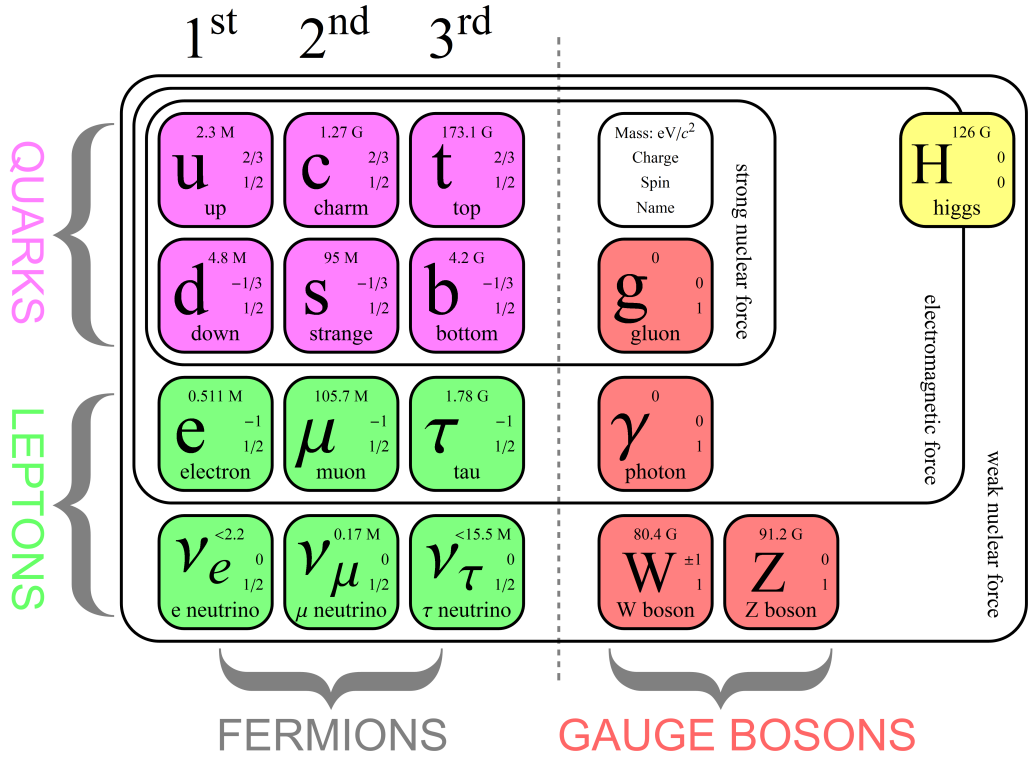

Figure 2: An overview of the elementary particles in the Standard Model. [4]

Lastly, the spin-0 scalar boson is known as the Higgs boson. Being the newest addition to the SM, the Higgs mechanism is predicted to assign mass to particles [6]. It plays an important role in the electroweak symmetry breaking (unification of the electromagnetic and weak interactions), explaining why $Z^0/W^{\pm}$ bosons acquire mass, unlike the massless photon.

2.2 QCD & Hadrons

QCD is a framework that describes the mechanics of the strong interaction, as well as fundamental theory regarding quarks and gluons. As previously mentioned, each of the six quarks has its own unique mass, as well as an electrical charge of either (opposite for anti-particles) $\frac{1}{3}e$ or $-\frac{2}{3}e$ (e being the elementary charge[1]). Alongside the electrical charge, the quarks and gluons (collectively called partons) also have a color charge, which is a unique feature of these particles. Instead of merely being positive or negative, the color charges come in three different flavors, with their respective anti-particle version: Red, Green and Blue. Similar to how a photon couples to the electromagnetic charge in QED, the gluon couples to the color charge in QCD. These color charges were originally introduced in order for the quarks to satisfy the Pauli exclusion principle, in the case of the Δ^{++} baryon[2]. This phenomenon gives rise to a notion that is referred to as color confinement, where individual colored particles cannot be observed [8].

However, a large difference between the mediators of QCD and QED is that the gluon can carry a charge of what it mediates (color), whereas the photon can not. Thus, it is possible for the gluon to interact with itself. The quarks and the anti-quarks carry single colors and anti-state colors respectively. The gluons, however, carry both a color and an anti-color. As the gluon interacts with other gluons and quarks, the color charge always remains conserved.

The strength of the strong interaction increases the farther the interacting quarks are from each other. This phenomenon is known as asymptotic freedom [10].This is due to the gluons ability to self-interact, which gives rise to an effect known as anti-screening. The effect is known from QED, where electrons and photons are able to screen each other due to quantum fluctuations, such as loops from pair production and annihilation. However, in the case of QCD, it is possible for the gluons to self-interact during such a quantum fluctuation. This process can be seen in Fig. 3. The probability of the gluons to self-interact, increases as the distance between the quarks increases. An increased probability to release radiation

[1] $e = 1.602 \cdot 10^{-19} C$ [7]
[2] Δ^{++} consists of 3 up quarks with parallel spin

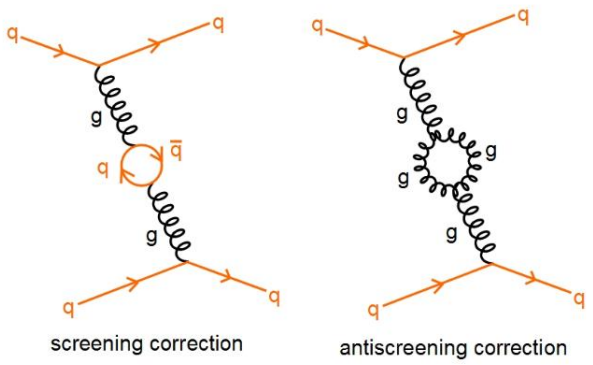

Figure 3: An illustration of the anti-screening process in QCD [9].

means that the total color concentration in each quark is increased [11]. This effect will cause the surrounding quarks to become 'anti-screened', and will start to notice surrounding charges. An increase of color concentration means that each quark will behave more like free particles, hence the strength of the strong interaction is decreased over short distances [12].

The coupling constant for the strong interaction, α_s is often used in order to gauge the behavior of the strength for the strong interaction. α_s is defined as follows:

$$\alpha_s(Q) = \frac{16\pi^2}{11 - \frac{2}{3}N_f \ln[\frac{Q^2}{\Lambda^2}]} \tag{1}$$

where Q is Lorenz invariant generalization of the momentum transfer in the interaction [13], N_f the number of quarks that can partake in the screening loop and Λ a scale parameter that is chosen such that the coupling constant is calibrated at the mass of the Z^0 boson (approximately 0.2 GeV) [14].

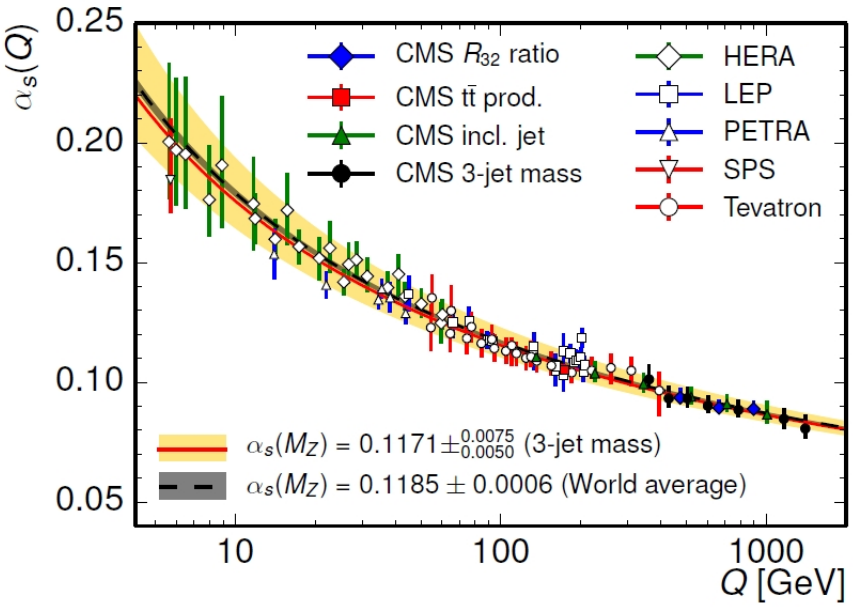

Figure 4: The running coupling constant for the strong interaction, as measured by various different high-energy physics experiments [15].

The running coupling constant can be seen plotted in Fig. 4, together with data from different particle interactions. It can been seen that the strong coupling constant not only qualitatively, but also quantitatively describes the two limits of color confinement and asymptotic freedom. QCD calculations can be done rather accurately for the region where asymptotic freedom dominates, using perturbation theory. However, similar calculations for the region where color confinement dominates are, at present, limited [8].

As previously mentioned, due to the color confinement, quarks and gluons can not be observed as free particles, but are instead bound in hadrons. The quark composition inside a hadron has to be such that the total color charge is neutral [16], as seen in Fig 5 . This ensures that hadrons can have more than one of a specific type of quark, and still not violate the Pauli exclusion-principle (such as the Δ^{++} having three up-quarks).

There are currently two types of hadrons; baryons and mesons. Baryons consist of a triplet of either three quarks or anti-quarks, whereas a meson consists of a quark - anti-quark pair. The electric charge can be either neutral or positive/negative, depending on the total sum of the electrical charge from the constituent quarks. However, the quark composition is always such that the total electrical charge is an integer number.

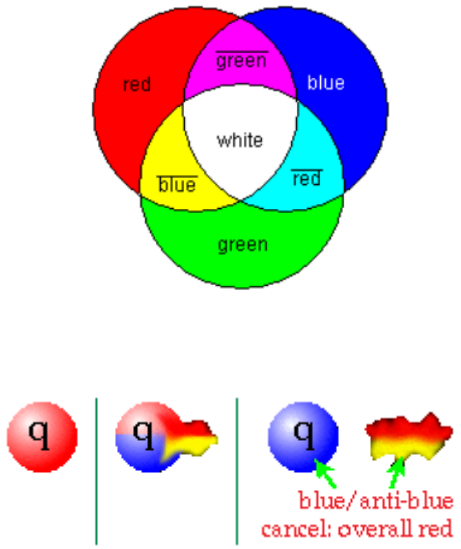

Figure 5: A figure illustrating the different colors for the strong interaction (top), as well as showing how the color flavor for a contained system, whilst emitting a gluon, is conserved (bottom) [17].

2.3 Proton-Proton Collisions

The particle collisions that were analyzed throughout this report were that of proton-proton (p-p) collisions. Understanding the underlying mechanics behind p-p collisions is important, as being the lightest baryon, it is the only stable hadron. As a p-p collision is simply two singular protons colliding, one can also view the event as a direct collision between partons within the hadrons.

A p-p collision (as well for most particle collisions) exhibits two different types of processes, hard scatterings & soft scatterings. The soft scattering is associated with collisions that have a small momentum transfer. During such collisions, the momentum transfer is sufficiently small to keep the partons bound inside the hadrons. Due to color confinement, the partons from each proton are essentially blind to each other, and the collisions are mostly elastic [18]. The soft processes are responsible for the color exchange between quarks, where gluon string fields are created between the interacting quarks (which is further discussed in Section 2.4). Soft interactions are accountable for phenomena such as bulk particle production & hydrodynamic flow [19].

In contrast, hard scatterings are associated with collisions with a large momentum transfer. As seen in Fig. 4, in section 2.3, the coupling constant decreases as the momentum transfer increases. Hence, the quarks behave almost like free particles during hard scatterings. Such collisions are highly inelastic, and the colliding particles (as well as those produced during the interaction) will scatter at large angles perpendicular to the beam-axis. Hard scatterings manifest themselves in phenomena such as jets (which is further explained in Section 2.4).

2.4 The Lund String Model

The Lund String Model attempts to describe how gluons and quarks create new hadrons during particle collisions. This process is referred to as hadronization. During a particle collision, the colliding quarks will start to form gluon color fields between each other. As the particles drift apart, more and more energy is contained within the color fields between them. In the Lund String Model, these color fields are approximated by 1-dimensional strings, with a string tension $\kappa = 1$ GeV/fm. If the quarks are separated enough, the string will reach a threshold energy sufficient to break the string, and will spontaneously create a new pair of quarks. This phenomenon can be seen illustrated in Fig. 5, with a quark (Q) - anti-quark ($\bar{Q}$) pair. A string can have multiple breakings, ending up in hadrons eventually.

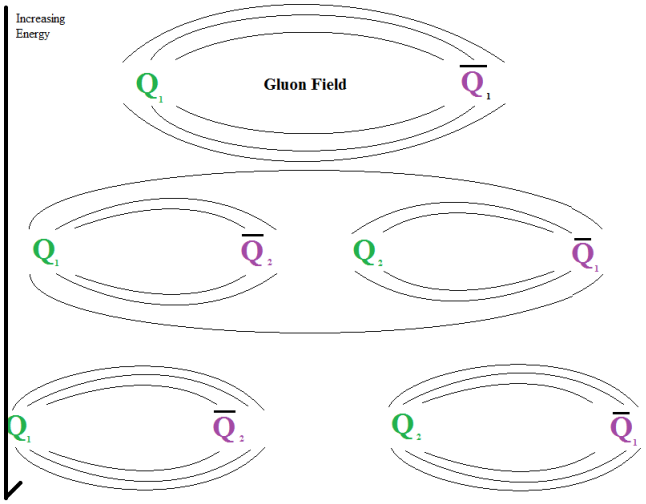

Figure 6: An illustration of the Lund Sting model, producing a $Q\bar{Q}$ pair as the gluon string field expands.

Hadronization is inherently a soft process, and occurs during every collision. As the quarks interact via gluon exchanges, a gluon color field will span and hadronization will occur (isotropically). However, if a hard scattering occurs during the process, large amounts of energy will be deposited into the color fields, enough to cause hadronization chain-reactions. As seen in Fig. 6, the two newly created $Q\bar{Q}$ pairs will have new gluon fields and create even more $Q\bar{Q}$ pairs. This will give rise to showers of hadrons that are called jets, which focus large numbers of hadrons into cones directed away from the beam-axis. During hard scatterings, as the incoming hadrons collide with a well-defined momentum along the beam-axis, two opposite jets, with opposite directions, are created in order to conserve momentum. Such a collision is referred to as a di-jet event. As the presence of jets is easily identifiable in particle detectors, and jets only occur during hard scatterings, the presence of a high-energetic jet can be used to deduct that hard processes occurred during that given collision.

2.5 Quark-Gluon Plasma

As previously explained, gluons and quarks can not exist freely, but have to be confined within hadrons due to color confinement. However, a state of matter was hypothesized where quarks and gluons could be deconfined from their individual hadrons. This new state of matter is called the Quark-Gluon Plasma (QGP). It is proposed that during the creation of the Universe, the matter in the Universe existed as a QGP for a few microseconds after the Big Bang. The idea is that, by increasing the pressure (merging the hadrons together) and heat (exciting the quarks out of the hadrons), the partons will merge together into one large quark-gluon 'soup', as seen in Fig. 7. It is believed that accelerated particle collisions at the LHC may provide enough heat and pressure during the initial collisions. This state of matter would thus be incredibly hot and dense.

However, the task to verify the creation of man-made QGP is a difficult one. In order to maintain a QGP, large amounts of continuous temperature and pressure would be needed to the system, as the QGP would else quickly cool down and re-confine back into hadrons. Thus it is not possible to create a stable QGP on a macroscopic scale, but its effects and existence must instead be observed by measuring auxiliary effects of the QGP medium.

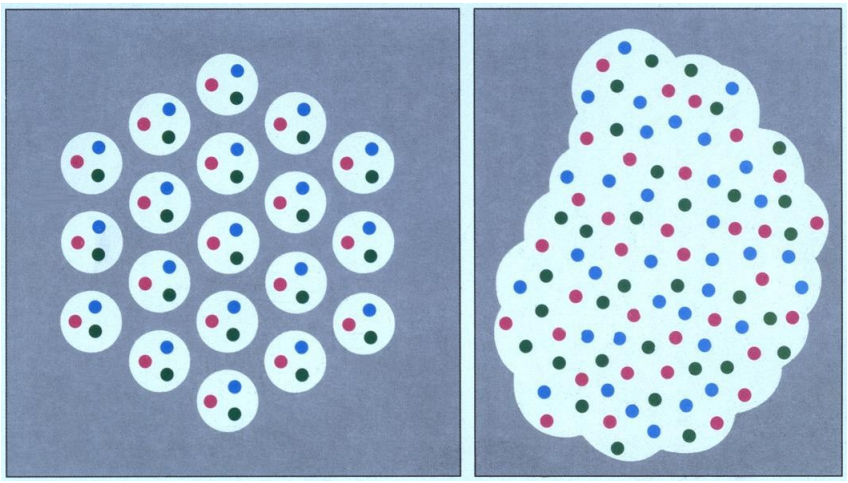

Figure 7: An illustration of isolated hadrons merging into a quark-gluon plasma

One of the believed characteristics of the QGP is strangeness enhancement. This was first proposed theoretically in 1980 [20], where collisions which created the conditions for QGP had a larger amount of 'strange' particles (hadrons containing s quarks) compared to collisions that did not create the conditions for a QGP phase. The strangeness enhancement, and the creation of the strange hadrons, can be described by a statistical Grand Canonical Ensamble, where the QGP is compared to a non relativistic 'hadron gas' in thermal and chemical equilibrium. The hadrons are able to merge together during the QGP-phase, forming new baryons and mesons, where the number of produced strange mesons rebalance to the number of produced non-strange mesons.

In heavy ion collisions, it has been found that there is a strangeness enhancement up to a factor of 10 in collisions where the QGP is expected, compared to collisions where it is not. This is attributed to the large gluon density within the QGP, as well as a lowered energy threshold required for the QCD processes that produce $s\bar{s}$ pairs. Additional reading on the specifics of the lowered energy threshold can be found here [21, 22]. Perturbative methods can be used in order to describe how strange particles are created in mid - to high transverse momentum (see Sec. 2.7.1), such as partonic scatterings, flavor excitation & gluon splittings [23]. However, the low transverse momentum-end is dominated by non-perturbative processes.

2.6 The ϕ Meson; Lund String Model Vs Hydrodynamic Models

A recent study performed by the ALICE collaboration [23] shows that there is strangeness enhancement of multi-strange baryons for high-energetic p-p collisions, similar to the effects found in heavy ion collisions. The results from this study can be seen in Fig. 8. The ϕ meson , consisting of a $s\bar{s}$ pair, is therefore interesting to study, as it does not consist of any up or down quarks (contained in the two protons colliding) brought into the collision, but instead of strange quarks created during the collision. As there are doubts whether p-p collisions create enough heat and pressure in order to create QGP, there are conflicting views on how the ϕ meson is dominantly produced.

According to the Lund String-like models, the ϕ meson is created by two $s\bar{s}$ string breakings, strings that are formed from the gluon string fields between quarks, as seen below in Fig. 9. The production of a single $s\bar{s}$ pair is suppressed, compared to the probability of creating u/d quarks, as the probability of string fragmentation P is proportional to the quark mass:

$$P \propto e^{\frac{-m_q^2}{\kappa}} \tag{2}$$

where m_q is the quark mass, and κ the string tension. As such, the creation of a ϕ meson should be double suppressed according to Lund string-like models. In hadronic systems (such as p-p collisions), where the phase space for particle production is limited, strangeness (a quantum number that every s quark and s anti-quark carries) conservation laws have to be implemented locally. Hence, the strangeness has to not be hidden in order to conserve. This is known as the canonical suppression of strangeness [22]. This claim is used in order to justify that the discrepancy of strange mesons between heavy ion collisions and p-p collisions is due to a suppression of strangeness in p-p collisions, rather than an enhancement of

strangeness in heavy-ion collisions (and is thus not considered as a signature of the QGP). The production of ϕ particles would be dominated by jetty, hard processes in such a model.

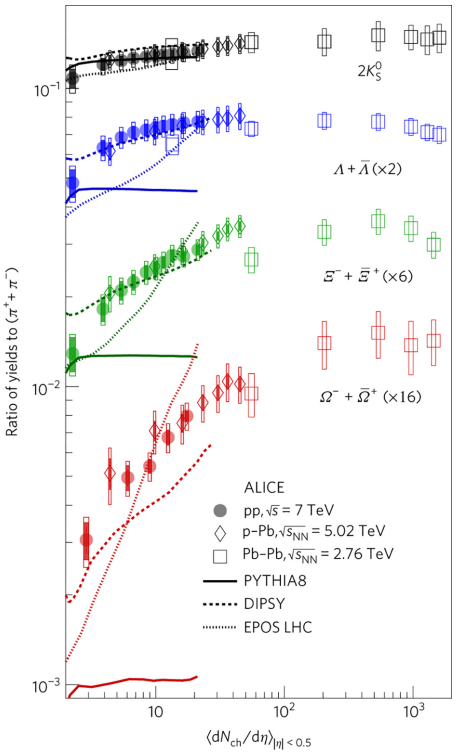

Figure 8: Results from a recent study from the ALICE Collaboration on enhanced production of multi-strange baryons in p-p collisions. The results are shown for a selection of event classes, with different particle collisions (see paper for more information)[23].

In contrast, according to hydrodynamic statistical models (as described by the Grand Canonical Ensamble), where the hadrons can merge together in order to form ϕ meson, the strangeness of the individual particles does not matter. Described by large particle systems, with several interacting particles, the chemical potential can be used in order to, on average, conserve the strangeness. The individual strangeness is therefore considered hidden and the ϕ meson is not canonically suppressed. As seen below in Eq. 3, the ϕ meson is not produced according to its quark mass in the hydrodynamic model, but to its total hadronic mass M_H, which is similar to that of a proton:

$$P \propto e^{\frac{-M_H}{\kappa}}. \tag{3}$$

In such models, the production of the ϕ are produced through soft processes as bulk particles, and would be spread out in an isotropic manner.

The double suppression from Lund String-like models put a constraint on the availability of ϕ mesons, whereas the statistical models do not. Thus, by further observing how the ϕ meson is produced in particle collisions, it should be possible to see which model fits the data best, and should result in understanding whether it is possible for p-p collisions to evolve towards a QGP phase or not.

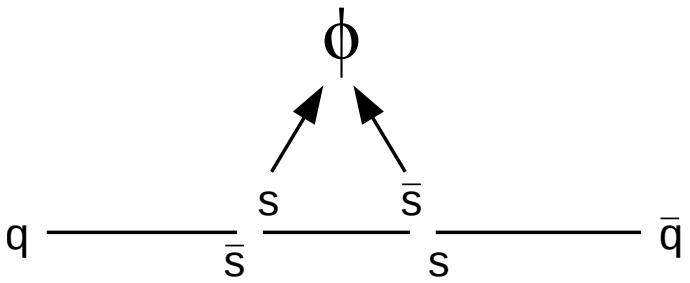

Figure 9: The creating of a ϕ meson by the breaking of two gluon strings [24]

2.7 Brief Overview of Basic HEP Phenomenology

2.7.1 Transverse Momentum

Particle detectors at colliders are often (but not always) built concentrically around the accelerator beam-axis in where the particles travel. Thus, the momentum component that is easiest to detect is the one that is transverse to the beam-axis. This is in turn referred to as the transverse momentum p_{T} of the detected particle, which is defined as:

$$p_{\mathrm{T}} = \sqrt{p_x^2 + p_y^2} \tag{4}$$

where p_x^2 and p_y^2 correspond to the momentum components of the two Cartesian coordinates, x and y, that are perpendicular to the beam-axis. As p_{T} will always be (approximately) zero for the incoming particles before the collision, the scattered partons and particles will always have a non-zero p_{T} after the collision. Thus, observing the p_{T} gives a a good insigt into the physics that occurred during the collision, e.g. measured jet production that can be associated to hard scatterings

2.7.2 Azimuthal and Polar angles

As previously mentioned, due to the specific geometric shape of the average HEP detector, spherical coordinates are used in order to describe where the scattered particles are detected. There are two key variables that are needed in order to describe the system. Firstly, the azimuthal angle φ describes the rotational angle across the x-y plane (assuming the beam-line is in the z-direction), in reference to some arbitrary point within that plane. As seen in Fig 10, one could imagine the azimuthal angle as the angle around the unit circle.

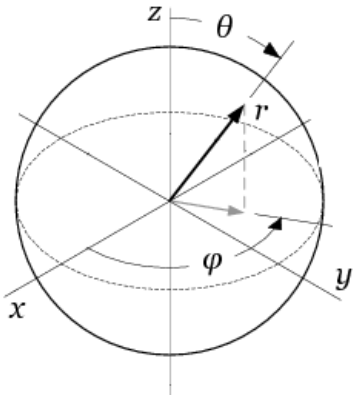

Figure 10: Example of how the different spherical angles φ and θ relate to regular Cartesian coordinates.[25]

On the other hand, the polar angle θ, also referred to as the scattering angle, describes the angle of inclination between the beam-line and the particle track. Combining measurements of the two angles for the same particle track, it is possible to define the location of a particle track in a full 3-dimensional space. Generally, the underlying physics in high-energy collisions is θ dependent, but has on average no φ dependence.

2.7.3 Rapidity and Pseudorapidity

In order to measure the longitudinal momentum components for each track, a new entity is introduced; the rapidity y, defined as[26]:

$$y = \ln \frac{E + p_z}{E - p_z} = \operatorname{arctanh} v_z \tag{5}$$

where p_z is the momentum component parallel to the beam axis, $E = \sqrt{m^2 + \boldsymbol{p}^2}$, which is the total energy of the particle, m is the mass, $\boldsymbol{p}$ is the total momentum vector, and v_z the velocity component of the particle along the beam-axis. Distributions measured as a function of rapidity are Lorentz additive for boosts along the beam-axis, and since the particles move at relativistic speeds, the rapidity is measured for the particles rather than the standard velocity. However, rapidity can be rather hard to measure, especially for highly relativistic particles. This is due to the fact that, as seen in Eq. 5, the mass is required to determine the rapidity. Therefore, an approximation of the rapidity is used, named Pseudorapidity (η):

$$\eta = \frac{1}{2} \ln \frac{|\boldsymbol{p}| + p_z}{|\boldsymbol{p}| - p_z} = -\ln \tan \left(\frac{\theta}{2} \right) \tag{6}$$

where $\boldsymbol{p}$ and p_z are defined like in Eq. (5), and θ is the scattering angle.

Pseudorapidity is a valid approximation for rapidity when the mass of the particle $m << p_{\mathrm{T}}$. In that case, the pseudorapidity will inherit the Lorentz additive invariance from the rapidity. Therefore, as there is a relation between the scattering angle θ and the pseudorapidity η (which can be seen in Fig. 11), η and φ are usually used to describe the cylindrical coordinates more often than θ and φ. This is due to that it becomes easier to perform a Lorentz boost on the data if the varible is Lorentz invariant. The various momentum components in Cartesian coordinates can thus be expressed as:

$$\begin{aligned} p_x &= p_{\mathrm{T}} \cos(\varphi) \\ p_y &= p_{\mathrm{T}} \sin(\varphi) \\ p_z &= p_{\mathrm{T}} \sinh(\eta) \end{aligned} \tag{7}$$

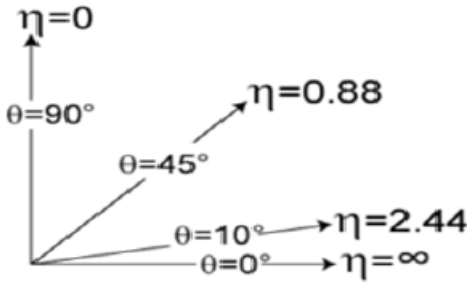

Figure 11: A figure displaying how η evolves with θ[27]

While the pseudorapidity is an excellent approximation for high-momentum particles, it does not perform as well for low-momentum particles. Therefore, a rapidity correction is needed in order to correct for the low-momentum particles in the various spectra that are functions of $\mathrm{p_T}$. This correction is further discussed in Sec. 4.2.2.

2.7.4 Jet Radius

The Jet Radius ΔR is a measurement for the difference in pseudorapidity η and azimuthal angle φ between two tracks. For two given tracks $t_1(\eta_1, \varphi_1)$ and $t_2(\eta_2, \varphi_2)$, ΔR is defined as:

$$\Delta R = \sqrt{(\varphi_2 - \varphi_1)^2 + (\eta_2 - \eta_1)^2} \tag{8}$$

ΔR is calculated between every pair of particles within the event, and is typically used in jet finding algorithms. In this study, it is used to characterize the shape of the event, and to see if there is any underlying correlation between the scattered direction of the particle pairs. An illustration of such cone can be seen in Fig. 12

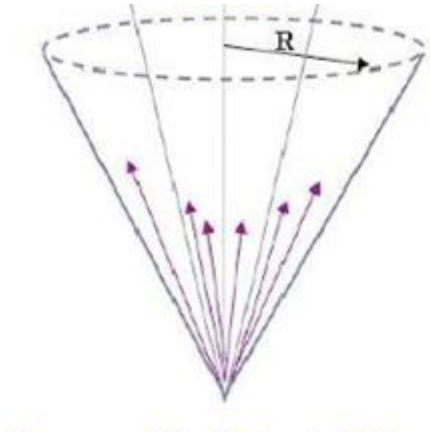

Figure 12: Illustration of the total jet radius R around a di-jet event. ΔR is then defined as the radius of cones between individual track pairs [28].

2.7.5 Multiplicity & Spherocity

The terms multiplicity and spherocity are both terms that are used in order to define important characteristics of individual collisions. Multiplicity is a term that refers to the number of particle tracks that are detected in a given collision. Collisions with a large multiplicity are indicative of a large momentum transfer during the collision, where the two particle bunches collide head on, and most likely contain jets (thereby having at least one hard interaction). On the other hand, collisions with a low multiplicity are indicative of a more glancing collision between the two particles, mostly containing soft interactions, and a small momentum transfer.

The transverse Spherocity S_0 is a variable used to define the overall geometric distribution of the transverse momentum p_{T} for the produced particles. It is defined as follows: [29]

$$S_0 = \frac{\pi^2}{4} \frac{\Sigma_i |p_{\mathrm{T}_i} \times \hat{n}|}{\Sigma_i p_{\mathrm{T}_i}} \tag{9}$$

p_{T_i} is the transverse momentum of a track in the event, and $\hat{n}$ is an arbitrary transverse vector in the x-y plane, that is chosen in order to minimize the S_0 ratio. The value of S_0 thus ranges between one and zero. Values towards zero are characterized as di-jet events, where the overall geometric shape of the events spike towards two opposite directions in the x-y plane. On the other hand, values of S_0 towards one represent isotropic events, where the produced particles are distributed evenly along the azimuthal angle, with similar values of p_T. The distinction between the two limits of S_0 is illustrated in Fig. 13. events that have a $S_0 \approx 0$ will henceforth be refereed to as "jetty" event, whereas events with $S_0 \approx 1$ will be referred to as "isotropic".

A recent study found that, using simulated particles created from the software PYTHIA (a program that generates high-energy particle collisions [30]), that there was a ϕ enhancement in isotropic events compared to jetty events [29]. These results are shown in Fig. 14, where the ratio of the measured numbers of kaons, protons and ϕ, to the number of measured π particles, is compared between different spherocities and p_{T} limits.

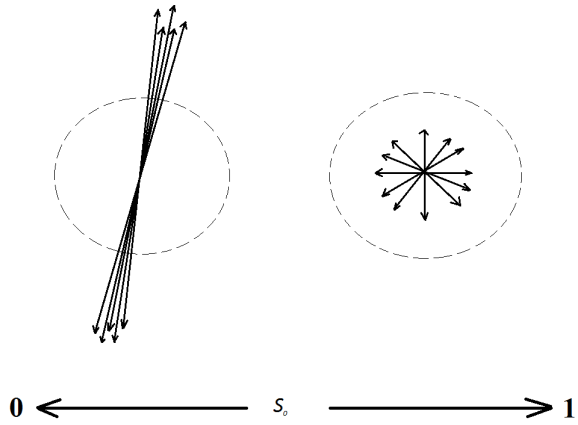

Figure 13: An example of two events that are towards the two limits of S_0.

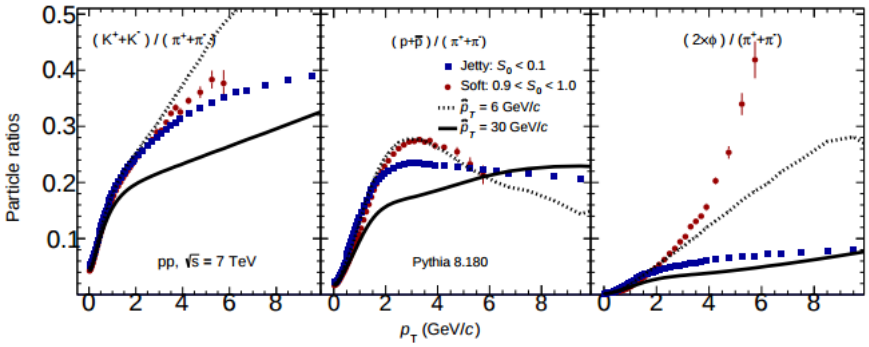

Figure 14: Results from a study, from Universidad Nacional Autónoma de México, where the yield of certain particles is compared to the yield of π mesons, for different spherocities [29].

2.7.6 Invariant Mass

The invariant mass, M_{inv}, also known as the rest mass, is a measurement of the mass that is invariant between different frames of reference. The term is derived from the expression the relativistic energy-momentum relation:

$$E^2 = \mathbf{p}^2c^2 + m_0^2c^4 \tag{10}$$

where E is the relativistic total energy, $\mathbf{p}$ the momentum four-vector as measured in any given reference frame, and m_0 the mass of a known set of particles. The invariant mass of the system is then:

$$M_{inv} = \sqrt{\frac{E^2}{c^4} - \frac{\mathbf{p}^2}{c^2}} = \sqrt{E^2 - \mathbf{p}^2} \tag{11}$$

where natural units ($c = 1$) are used in the last portion of the equation [31]. Throughout this report, M_{inv} will be used in order to describe the rest mass of the ϕ meson. This is done by calculating the M_{inv} between pairs of its decay products. As such, M_{inv} for a system of particles can the be written as:

$$M_{inv} = \sqrt{\Sigma E^2 - \Sigma \mathbf{p}^2} \tag{12}$$

where ΣE^2 and $\Sigma \mathbf{p}^2$ are the sum of the particles energy and momentum respectively. For a pair of tracks, $t_1(E_1, \mathbf{p}_1)$ and $t_2(E_2, \mathbf{p}_2)$, each with its corresponding momentum four-vector $\mathbf{p}$ = (p_x,p_y,p_z) the M_{inv} can thus be evaluated as:

$$M_{inv} = \sqrt{(E_1 + E_2)^2 - (\mathbf{p}_1 + \mathbf{p}_2)^2}$$
$$= \sqrt{(E_1 + E_2)^2 - ((p_{1z} + p_{2z})^2 + (p_{1y} + p_{2y})^2 + (p_{1x} + p_{2x})^2)} \tag{13}$$

3 Overview of the LHC

The Large Hadron Collider (LHC), at the European Organization of Nuclear Research (CERN), based in Geneva, is as of 2017, the worlds largest particle accelerator. Being a circular particle synchrotron, it contains 1000 superconducting magnets that bend the beam-line across its circumference of 27 km [32]. It is designed to accelerate and collide protons & ions in order to study the structure of fundamental particles, and how they interact with each other. The LHC can currently accelerate proton beams up to an energy of 6.5 TeV, which yields a 13 TeV center-of-mass energy once the two beams collide.

The LHC is fitted with several experimental stations throughout the beam-line that study the collisions. There are four main experiments; A Toroidal LHC Apparatus (ATLAS) and the Compact Muon Solenoid (CMS) being the two main general purpose detectors, whereas LHCb and A Large Ion Collider Experiment (ALICE) are specialized detectors (b-quark physics and heavy ion physics respectively). An overview schematic of LHC and the four main experiments can be seen in Fig. 15. The experiments each host their unique particle detectors, that are built differently and function through different means. As the detectors operate differently from each other, if the same behavior is reproduced in more than one detectors, it is possible to conclude that the observed signal is reproducible without detector bias.

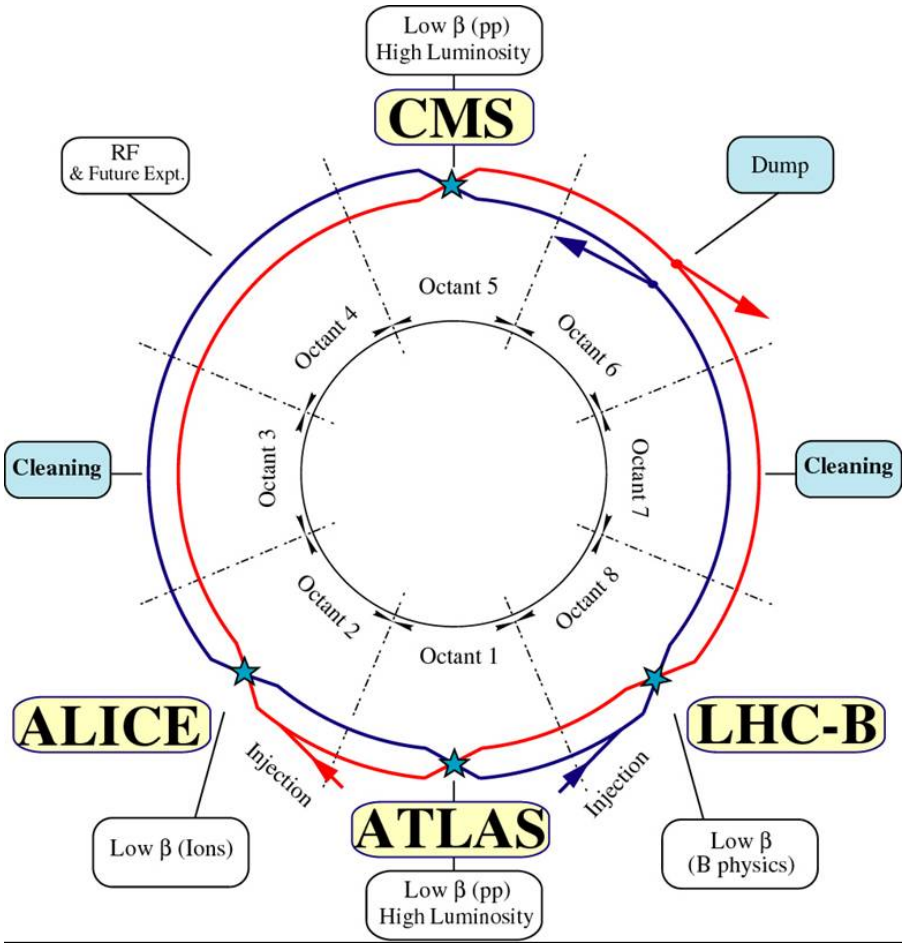

Figure 15: An overview of the LHC and its four main experiments [33].

3.1 The ALICE Detector

The data presented throughout this report is based on p-p collisions at a center-of-mass energy of 13 TeV, measured at the ALICE detector. Like most particle physics experiments, ALICE is built concentrically around the beam-axis. A full illustration of ALICE and all its various components can be seen in Fig. 16. The detector system has a full 2π azimuthal coverage around the beam-line. The η coverage is different for each detector component, and is illustrated in Fig. 17.

The different detector components that are shown in Fig. 16 each focus on measuring certain aspects of the produced particles. In regards to the collection of the data presented in this report, there are some

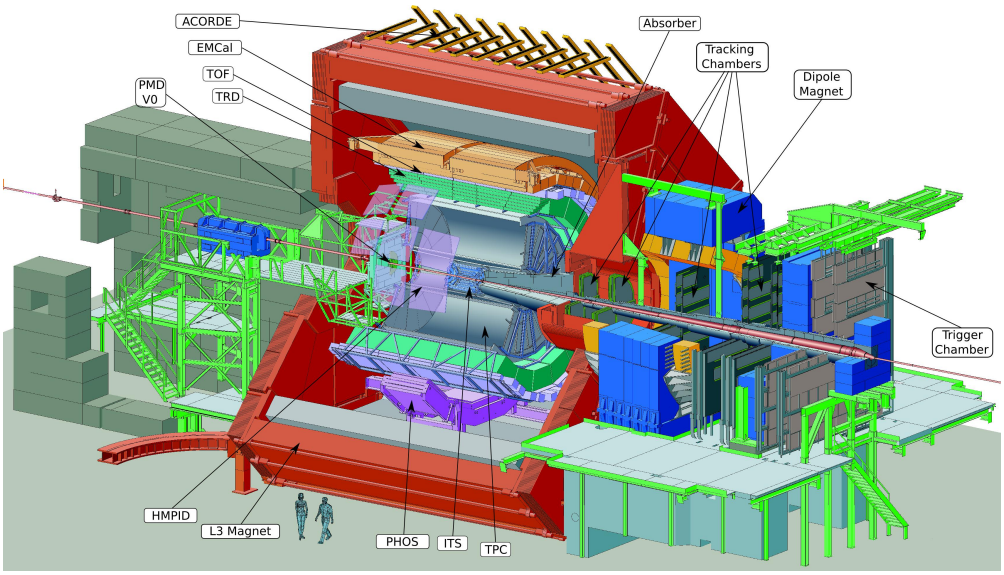

Figure 16: A figure displaying the ALICE detector, and its individual sub-detector components [34].

that are more relevant than others; the Time-Projection Chamber (TPC), the Time-of-Flight detector (TOF), the Inner Tracking System (ITS) and the V0 detector. Each of the these detectors will be covered in more detail.

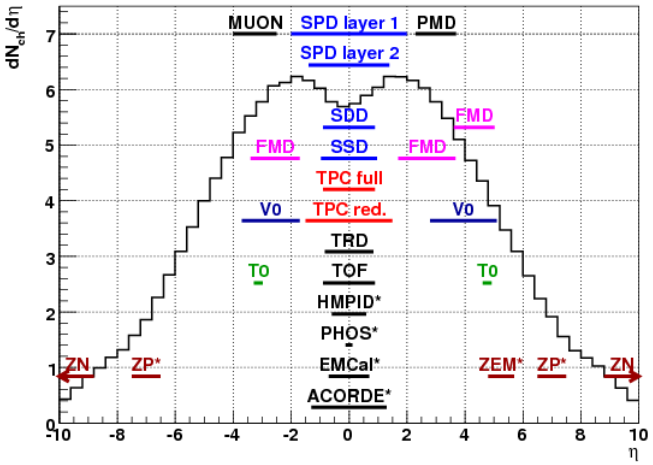

Figure 17: A figure illustrating the different η-acceptances for each sub-detector system in ALICE [35].

3.1.1 Time-Projection Chamber

The Time Projection Chamber (TPC) is the main tracking chamber of ALICE. The TPC is tasked with tracking & reconstructing the spatial location of the individual particle tracks. A basic overview of the detector can be seen in Fig. 18. The TPC is a symmetrical, hollow cylinder that is fitted co-axially with the beam-line. As the drum has a gas volume of 88 m^3, and is filled with a gas mixture of 90% Ne and 10% CO_2 [37]. As the charged particles traverse the gas, the atoms in the gas will ionize. An electric field is applied across the drum, parallel to the beam-axis, so the the electrons released from the ionization will drift along the applied electrical field. Thus the gas mixture acts as a drift gas for the incoming particle tracks. With a maximal drift length of 2.5m, and a drift field of 400 V/cm, it takes 88μs for the electrons to drift from the central HV electrode to the end-plates of the TPC [38].

The end-plates of the TPC contain cathode planes of Multi-Wire Proportional Chambers (MWPCs). Once the drifting electrons reach the end-plates, the MWPCs will amplify the signals through a chain of electron avalanches. The final signal is then read out, and translates into the two spatial coordinates

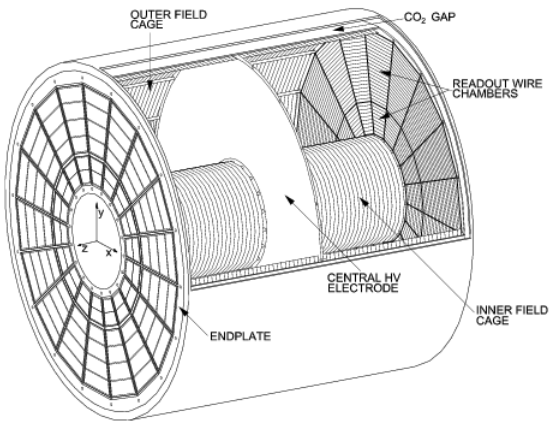

Figure 18: A figure illustrating the ALICE TPC [36].

(x,y). The z-component is found by measuring the drift time (the time it takes for the ionized electrons to drift through the gas) of the particle.

As the TPC can measure the three Cartesian coordinates of a particle track, it is possible to obtain the transverse momentum of each track by applying an external magnetic field B, parallel to the beam-axis, with a strength of 0.5 T [39]. This is done by measuring the gyro radius ρ of the particle track, which is a measurement of the particle's curvature due to the external magnetic field:

$$B \cdot \rho = p_{\mathrm{T}}/q \rightarrow p_{\mathrm{T}} = B \cdot \rho \cdot q \tag{14}$$

where p_{T} is the transverse momentum of the particle track, and q the charge of the particle track.

The applied magnetic field also helps to constrain the signal resolution. There is a very large probability for the drifting electrons to interact with other atoms during the drift. Hence the signal can be considered point-like as the particle track starts the ionization, but will spread out with a statistical uncertainty as the signal approaches the MWPC. The magnetic field will force the electron to spiral through the gas, preventing it from straying off further. The internal magnetic and electric field created by the drifting current itself are negligible compared to the parallel external fields.

Furthermore, aside from measuring the spatial coordinates and the momentum of a given particle track, the TPC can also identify which kind of particle the detected track corresponds to. It does so by measuring the energy loss per distance (also referred to as the stopping power), $\frac{\mathrm{d}E}{\mathrm{d}x}$ (where $\mathrm{d}E$ are decrements of energy, and $\mathrm{d}x$ increments of length), as a function of the magnetic rigidity, p_{T}/q. By plotting these two physical quantities against each other, one will obtain a spectrum with distinct, discrete curves. Each of these curves then corresponds to a specific particle mass, making it possible to identify the particle track in question. Such a $\frac{\mathrm{d}E}{\mathrm{d}x}$ plot can be seen in Fig. 19. The mass for each particle is then identified using the Bethe-Bloch formula, which is defined as follows [40]:

$$-\frac{\mathrm{d}E}{\mathrm{d}x} = \frac{DZ^2 n_e}{\beta^2}\left[\ln\left(\frac{2m_e c^2\beta^2\gamma^2}{I}\right) - \beta^2 - \frac{\delta(\gamma)}{2}\right] \tag{15}$$

where Z is the atomic number $\beta = \frac{v}{c}$, $\gamma = \sqrt{1-\beta^2}$, m_e the electron mass, n_e is the electron density of the absorber, I the mean ionization potential[3] and $D = \frac{4\pi\alpha^2\hbar}{m_e}$ The important aspect of Eq. 15 is that the energy-loss is directly proportional to the mass of the incoming particle. The fitted red lines seen in Fig. 19 are calculated using the Bethe-Blochf formula.

While the TPC is designed to give good resolution for high multiplicity events, the setup requires longer intervals between collisions. This is due to that it requires a certain amount of time between each pulse to reset drift gas within the chamber. Before a new collision can be measured, the positive ions (produced due to the electron avalanches created in the MWPCs) have to drift back and neutralize on the cathode or gating grid, so that they do not make it into the drift gas. Thus the TPC is more suited to collisions that may contain a large amount of particle tracks, but under a lower collision rate.

[3] $I = 10\ Z$ eV for Z greater than 20

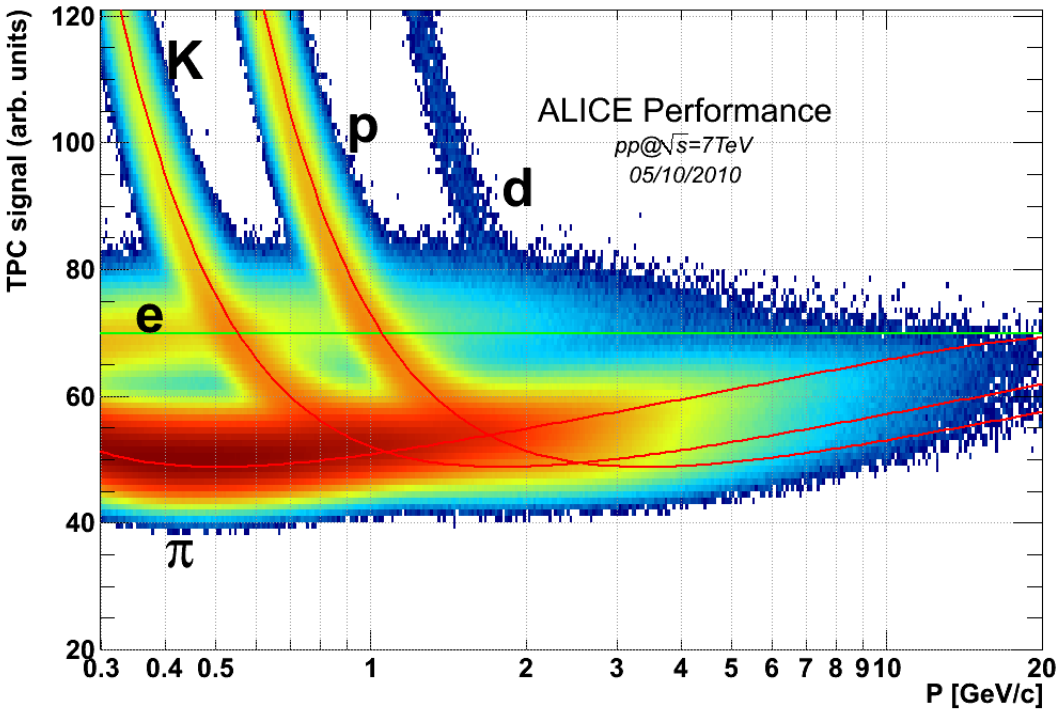

Figure 19: A typical TPC dE/dx plot, used in order to identify different particles that are created after a particle collision [41].

3.1.2 Inner Tracking System

In addition to the TPC, the Inner Tracking System (ITS) is essential to obtain a precise measurement of the p_{T} for a given particle track. The ITS is located before the TPC, and its main purpose is to give space points for each particle track, which helps in the global tracking of the collisions. It can track the particles precisely to the interaction vertex (in particular to be able to identify secondary decays of weak decays (heavy quarks). Additionally, the ITS can even track particles on the low-end of the momentum scale, around around 0.1 GeV/c and under.

The ITS complements the TPC to give ALICE a good estimation of the momentum for each particle, from the low-end to the reasonably high-end (60-100 GeV/c) of the momentum spectra.

3.1.3 Time-of-Flight Detector

The main purpose of the Time-of-Flight (TOF) detector is to identify charged particles by (in conjunction with the TPC) determining their mass. It does so by measuring the time it takes, for a particle track to travel from the initial interaction vertex (collision), to the registered hit in the TOF detector. Just like the TPC, the TOF Detector consists of a hollow cylinder, with full azimuthal coverage, as can be seen in Fig. 20. The shell is divided up several sectors, fitted with a total of 1638 Multigap Resistive Plate Chambers (MRPCs). The MRPCs are constructed by a stack of resistive glass plates, separated by 5 gas gaps (gas consists of a mixture of SF_6 and $C_2F_4H_2$) of 250 μm, which has an applied external voltage over it [42]. This separation is held constant by wedges made out of nylon fishing line. Once a charged particle travels through the two glass plates, it will ionize the the gas between them. The electrical field induced by the external voltage will then amplify the ionization, generating an electron avalanche. This avalanche then halts once it reaches one of the resistive glass plates, and the signal is picked up by read-out electrodes. The total signal is then represented by the sum of the read-out electrodes from each gap.

The design of the MRPCs are constructed in such a way that any time jitter, or any other defect caused by the diffusion process between the glass plates, is kept to a minimum. This is due to the small gap between the plates not giving much room for the ionizing electrons to spread out. Hence, the time resolution of the TOF signal is considerably accurate, lying around 100 ps.

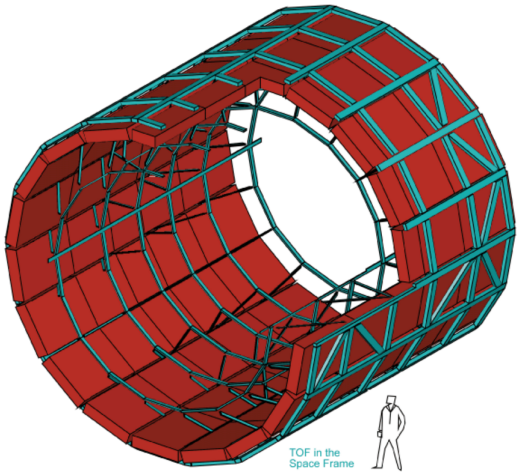

Figure 20: An overview image of the TOF detector [42].

Furthermore, once the time-of-flight for a particle track is measured, it is then possible to (in conjunction with the TPC) identify which type of particle has been detected. Under the assumption that the particle travels near the speed of light, measurements of Gaussian unfoldings of time-of-flight, the particle trajectory & the particle momentum makes it possible to fit a corresponding particle mass to the given track[43]. A characteristic combined TOF-TPC particle identification fit can be seen in Fig. 21.

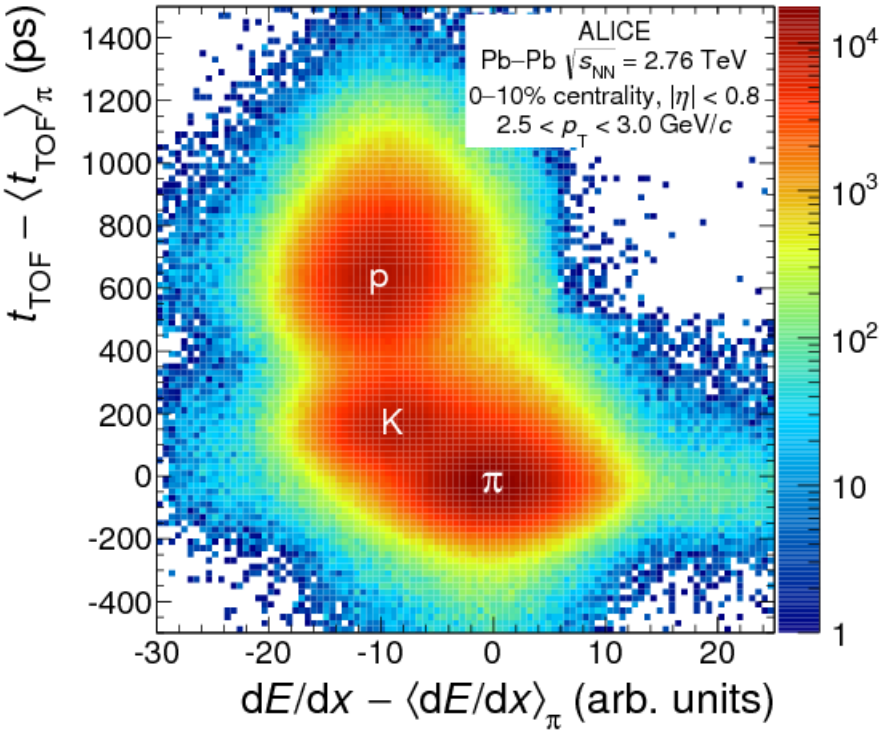

Figure 21: Particle Identification, combining both the time-of-flight and the $\frac{dE}{dx}$ energy loss [43].

3.1.4 V0 Detector

The V0 detector is mainly designed to measure the collision rate of the beam, as well as the multiplicity of charged particles after the collisions. The V0 detector consists of a pair of sub-set detectors; the V0-A, and V0-C. They are oppositely situated in the two far η regions, with V0-A covering $2.8 < \eta < 5.1$, and V0-C covering $-3.7 < \eta < -1.7$. The V0 detectors are discs that consist of different sectors of plastic scintillator detectors, as can be seen in Fig 22. Once a charged particle hits one of the V0 sectors, the plates will scintillate. As the scintillating detector is connected to a Photon-Multiplier Tube (PMT), the flashing light will be registered and amplified by the PMT, which is then able to be read out as a signal [44].

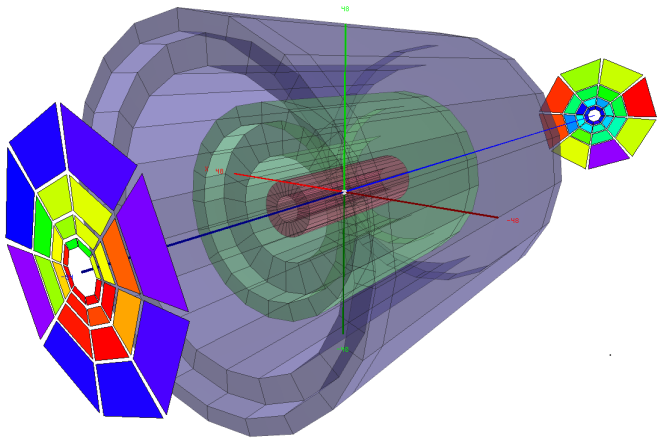

Figure 22: A figure displaying the two V0 detectors, their different sectors, and how they are located in relation to the TPC and TOF detectors [45].

The V0 detector acts like a minimum bias trigger; it triggers and detects tracks on the most basic level possible, in order to eliminate as much detector bias as possible, whilst still trying to reject candidates for possible "fake" signals (such as beam-gas scattering, see [46] for more detail). In this study, the V0 detector will mainly be used in order to gauge the multiplicity for each event. This can be done as the sum of amplitudes for the signals measured by the V0 detector are directly proportional to the multiplicity in each event.

4 Method of Analysis

4.1 Software & Tools

The analysis presented throughout this report was constructed in C++, using the ROOT data analysis framework [47]. Furthermore, a custom environment of ROOT was employed in order to calculate the different particle cuts, AliROOT [48], specifically designed for the ALICE collaboration. The simulation and reconstruction of simulated particles was done using two different programs. PYTHIA was used in order to generate the various particle interactions, and Geant4 [49] used in order to transport the generated particles, and simulate the detector conditions and triggers in used in ALICE.

4.2 Signal and Background Analysis

The purpose of this analysis is to measure the yield of ϕ mesons created in p-p collisions, between different multiplicities and spherocities, in order to search for any signs of ϕ meson enhancement. The main particle interaction that has been studied throughout this analysis consists of two stages of particle interactions. The two stages are the following:

$$\begin{aligned} &p + p \rightarrow \phi + X... \\ &...\phi \rightarrow K^+ + K^- \end{aligned} \tag{16}$$

where we collide two protons in order to create a ϕ resonance, along with a cluster of "unwanted" particles X. The ϕ meson may then decay into two kaons with opposite charge. Due to its short lifetime, the detector cannot directly detect the ϕ meson. However, the detector is able to detect the kaons, and it is therefore possible to indirectly reconstruct the ϕ meson by calculating the invariant mass M_{inv} of the kaon pair.

As the kaons cannot be individually picked out from the events (although they can be filtered to some extent, see Sec. 4.2.4), every particle track has to be considered a kaon for the M_{inv} calculation. This means that the M_{inv} distribution will contain lot of background due to kaon pairs that are not the result of a ϕ resonance, from combinatorial pairs (kaon pairs with different ϕ mother particles), and pairs that are misidentified as kaon pairs. Thus, in order to get a good estimation of the number of measured ϕ mesons, the ϕ meson signal has to be extracted from the background.

4.2.1 Event-Mixed Combinatorial Background

The combinatorial kaons might be correlated with the ϕ resonance. As such, it is preferable to make certain that the background is completely uncorrelated to the signal. To this end, event-mixing is in order to obtain a suitable background, where M_{inv} distributions are reconstructed for kaon pairs between different events. This ensures that the two kaons constituting the background distribution are in no way correlated. In total, four different M_{inv} distributions, across several different p_{T} intervals, are used:

- Unlike-Sign Same-Event (USSE): Distribution of M_{inv} with tracks that have opposite charge, within a single event. This is the main distribution that contains the signal
- Like-Sign Same-Event (LSSE): Background distribution of M_{inv} with tracks that have the same charge, within a single event.
- Unlike-Sign Mixed-Event (USME): Background distribution M_{inv} with tracks that have opposite charge, each from a different event.
- Like-Sign Mixed-Event (LSME): Background distribution of M_{inv} with tracks that have the same charge, each from a different event.

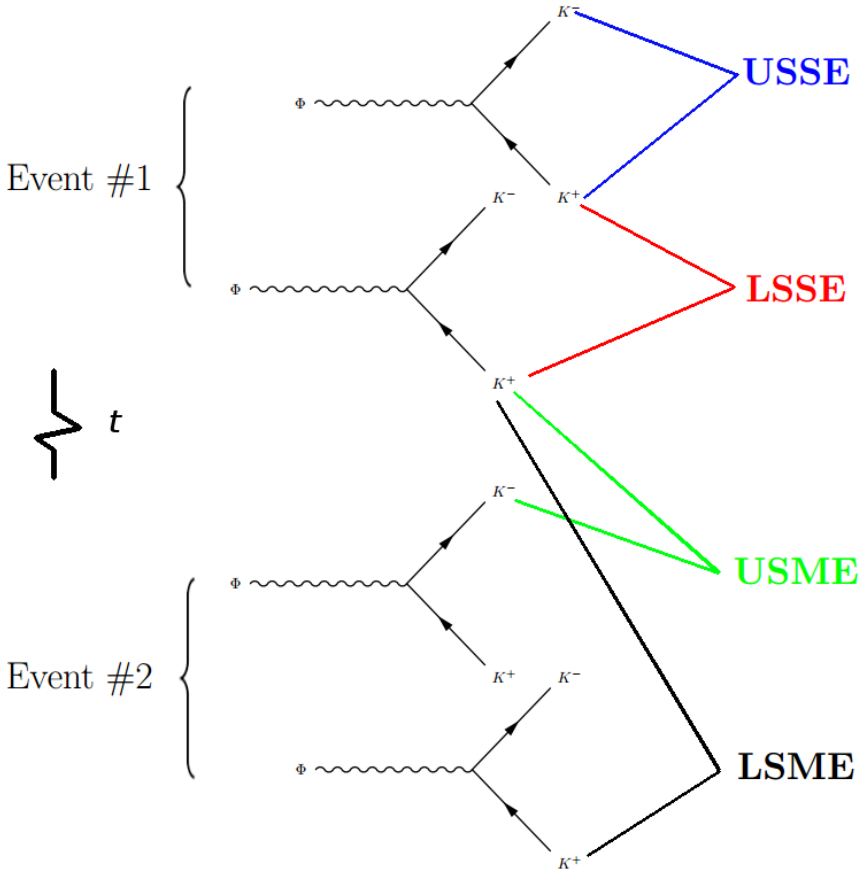

Figure 23: A rough illustration of the four invariant mass distributions. Event #1 and Event #2 are disjointed in time.

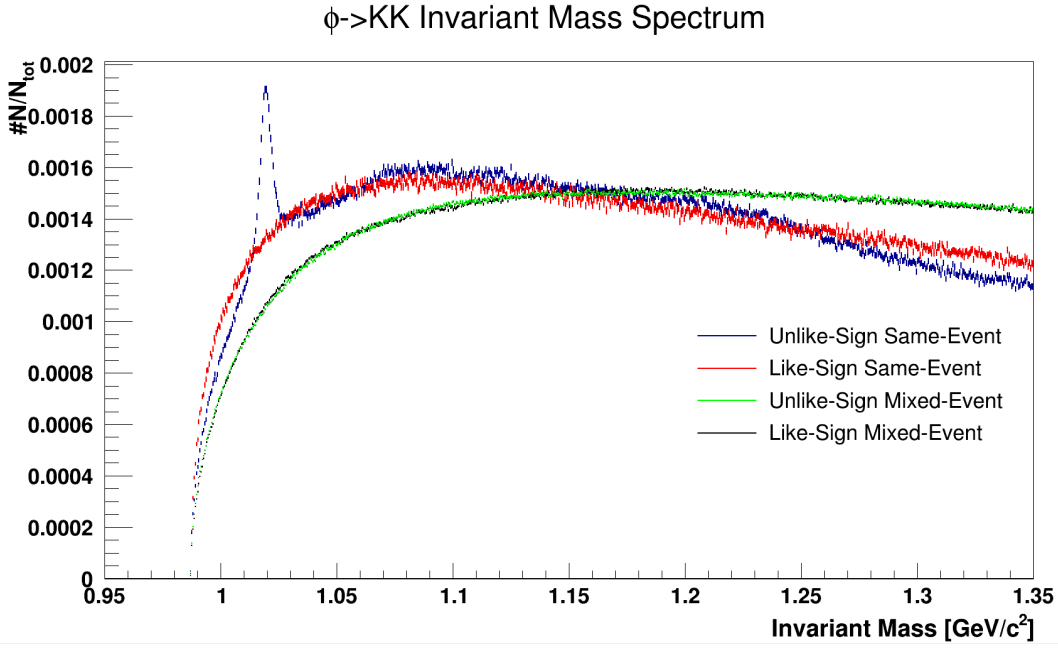

Figure 24: M_{inv} distributions obtained using USSE, LSSE, USME & LSME techniques, normalized to their respective entries N_{tot}, within a 2 GeV/c< p_{T} <4 GeV/c interval.

An example of these four invariant mass distributions is shown in Fig. 23. The USSE distribution will thus contain the ϕ meson signal, and be the main signal distribution throughout this thesis. The LSSE contains kaons that are charged equally, making certain that they do not originate from the same ϕ mother. Comparing USSE and LSSE is non-optimal, due to the risk of correlation between USSE and LSSE, as well as K^+ and K^- having different acceptance regions. Although the effect of this is most likely small, it would still induce a bias when comparing LSSE with USSE. Observing Fig. 24, one can clearly see that there is a difference between LSSE and USSE (disregarding the ϕ signal).

The USME & LSME both represent the uncorrelated, event-mixed background distributions. It is preferable to use USME as a background distribution to directly compare the USSE, as they both contain opposite charged kaon pairs. Hence, the USME background will be completely uncorrelated, while still retaining the same detector effects & acceptance as the USSE. For this analysis in particular, the two mixed-event distributions are acquired by mixing all kaons in each event, with kaons from with the 10 previous events.

4.2.2 Event Reweighing

As seen in Fig. 24, backgrounds for USSE and USME differ. This discrepancy can be understood more clearly if the invariant mass equation, M_{inv}, for the mixed events is written in full. For a two particle system, as described in Sec. 2.7.6, the tracks $t_1(E_1, \mathbf{p}_1)$ and $t_2(E_2, \mathbf{p}_2)$, each from a different event, the M_{inv} will then equal:

$$\begin{aligned} M_{inv} =& \sqrt{(E_1+E_2)^2 - ((p_{1z}+p_{2z})^2 + (p_{1y}+p_{2y})^2 + (p_{1x}+p_{2x})^2)} \\ =& \sqrt{(E_1+E_2)^2 - ((\sinh(\eta_1)+\sinh(\eta_2))^2 + (\sin(\varphi_1)+\sin(\varphi_2))^2 + (\cos(\varphi_1)+\cos(\varphi_2))^2)} \\ =& \sqrt{(E_1+E_2)^2 - \left(4\sinh^2\frac{\eta_1+\eta_2}{2}\cosh^2\frac{-\Delta\eta}{2} + 4\sin^2\frac{\varphi_1+\varphi_2}{2}\cos^2\frac{-\Delta\varphi}{2} + 4\cos^2\frac{-\Delta\varphi}{2}\cos^2\frac{\varphi_1+\varphi_2}{2}\right)} \end{aligned} \tag{17}$$

As seen in Eq. 17, M_{inv} is dependent on differences in the azimuthal angle $\Delta\varphi$. This can lead to large irregularities in M_{inv}, if at least two events with large jet activity are mixed. The mixed event is then no longer necessarily characterized as a di-jet event, as seen in Fig. 25. Hence, the event-mixing creates a background distribution that is not necessarily representative of the supposed background that exists within the same-event signal. This can be clearly seen in Fig. 26, where the values for $\Delta\varphi$ is measured between same-events and mixed-events.

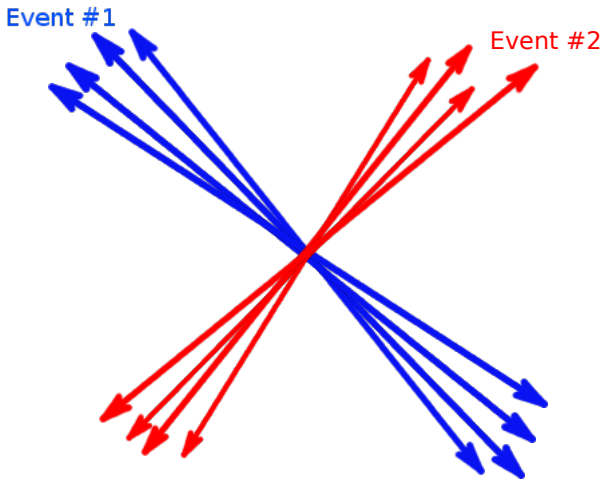

Figure 25: Two mixed events with perpendicular di-jet angles. Events #1 and #2 are disjointed in time, and represent data from two different collisions.

Since the ϕ meson resonance cannot exist in either of the LSSE or LSME distributions (due to both containing only same-sign kaons), they will be used in order to correct for the difference in topology between the same-event and mixed-event spectra. The first step is to measure a ΔR distribution for

LSSE and LSME, such that both ΔR and M_{inv} distributions are created for the same p_{T} interval. Observing Fig. 27 a clear difference of ΔR is observed between the same-event and mixed-event like-sign backgrounds. A ratio between ΔR_{LSSE} / ΔR_{LSME} is used as reweighing ratio to renormalize USME to USSE. The effects of the reweighing can be seen down below in Fig.28, and will be discussed more in-depth throughout Sec. 5.

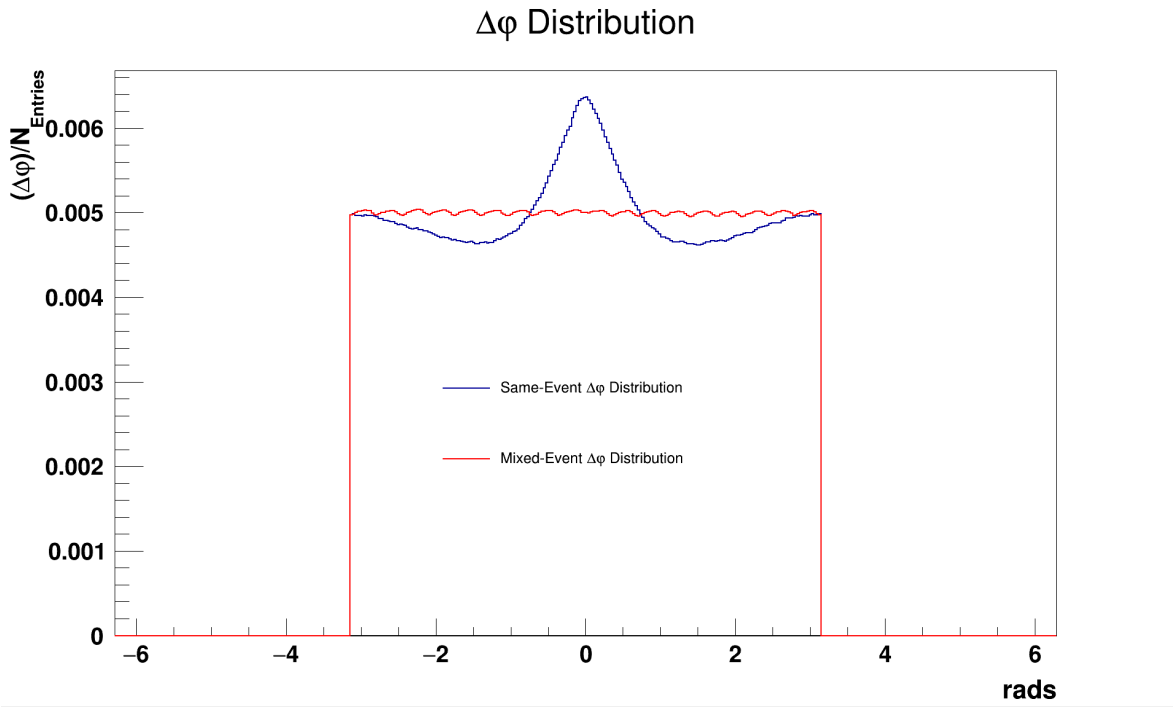

Figure 26: The difference in $\Delta\varphi$ distributions between same-event collisions and mixed-event collisions, within a 2 GeV< p_{T} <4 GeV interval.

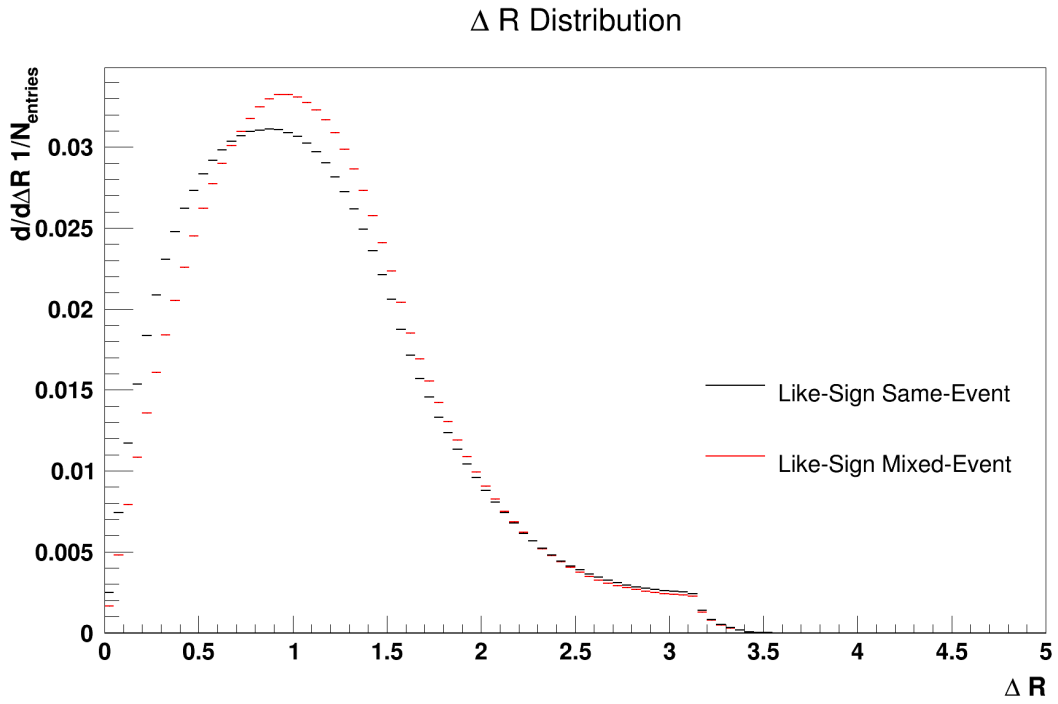

Figure 27: ΔR distributions connected to the LSME and LSSE distributions, within a 2 GeV< p_{T} <4 GeV interval. The cut-off at $\Delta R \approx \pi$ reflects the ALICE acceptance: $|\Delta\varphi| < \pi$ and $|\Delta\eta| < 1.6$

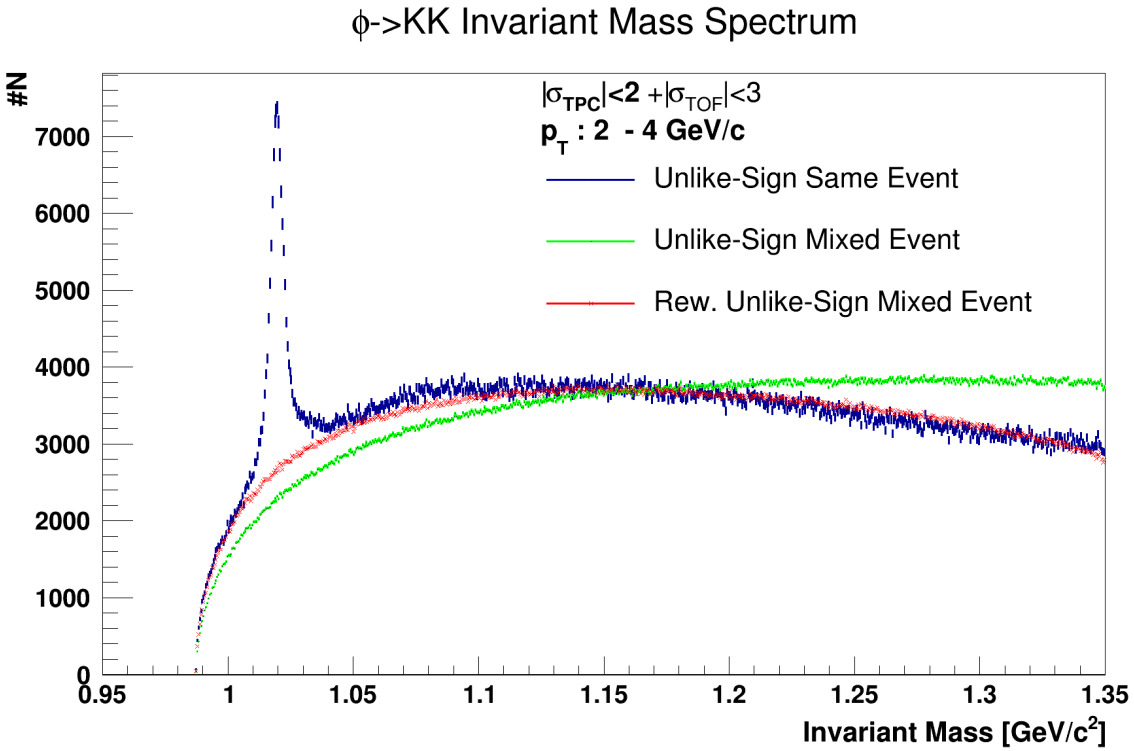

Figure 28: The difference between USME & Rew. USME background distributions compared to the USSE signal distribution, within a 2 GeV/c< p_{T} <4 GeV/c interval, normalized to the 1.15< M_{inv} <1.20 region.

4.2.3 Raw ϕ Yield & Relativistic Briet-Wigner Fit

In order to precisely determine the yield of ϕ mesons, once the reweighed background has been subtracted from the signal, yields are extracted from a fit to the data. A 2 degree polynomial background fit is applied to the reduced (USSE − Rew. USME) distribution:

$$B(x) = A + Cx + Dx^2 \tag{18}$$

where x represents the data points in the M_{inv} spectrum, and A, C and D are fitting parameters.

The signal distribution requires a more complicated fit in order to converge to the data. Therefore, a relativistic Breit-Wigner (BW) distribution is used in order to describe the data, which is defined as:

$$S(x) = \frac{2}{\pi} \frac{\Gamma^2 M_{phi}^2}{(x^2 - M_{phi}^2) + x^4(\Gamma^2/M_{phi}^2)} \tag{19}$$

where x represents the calculated M_{inv} data points, and Γ and M_{phi} are the width and the mean of the peak respectively. Values for M_{phi} were fixed to a constant value from the Particle Data Group[4][50] in order to make the fit converge in a smooth manner. The performance of the fitting procedures is seen in Fig. 29 across a 2 GeV/c < p_{T} < 4 GeV/c interval. Once the two distributions are fitted, the raw ϕ yield is attained by subtracting the background integral from the total signal integral.

[4] $M_{phi} \approx 1.019455$ GeV/c

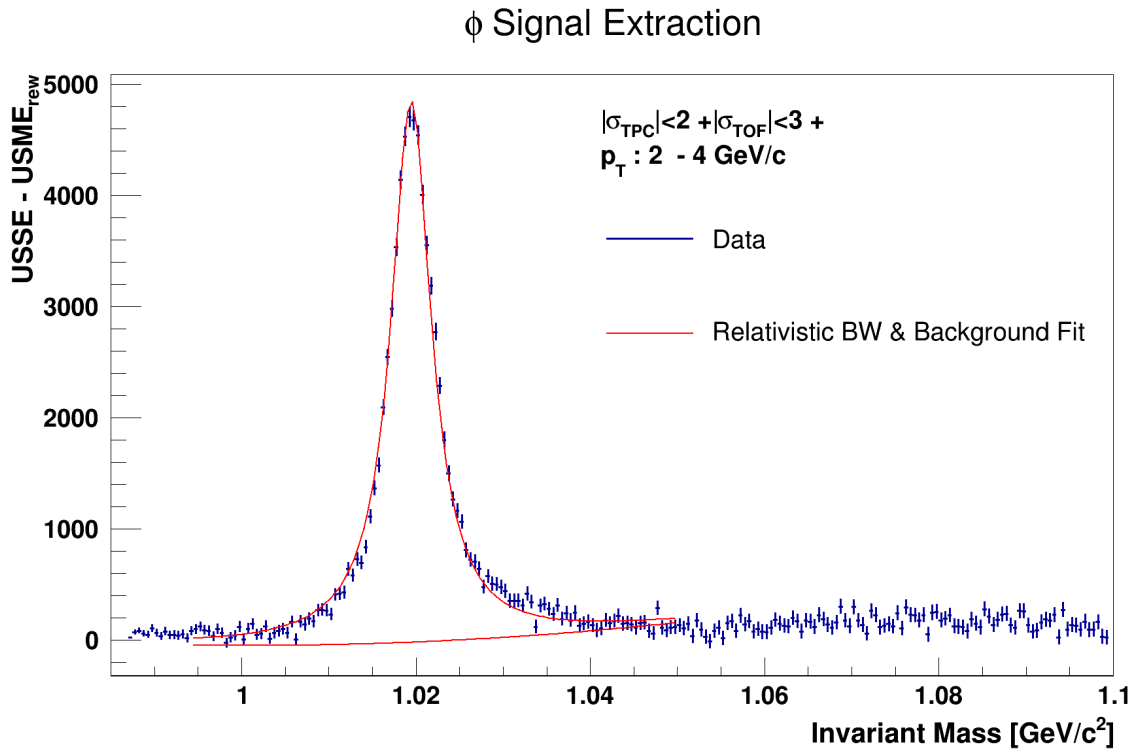

Figure 29: Signal and background distribution with a fit function for the reduced USSE spectrum, within a 2 GeV$< p_{\mathrm{T}} <$4 GeV interval.

4.2.4 Particle Identification & Kinematic Cuts

The four different (M_{inv}, p_{T}, ΔR)-distributions are further divided into several sets. The sets are distinct from each other in that they contain different cuts that try to remove particles that can not be identified as kaons, referred to as Particle Identification (PID) cuts. However, while the cuts increase the probability that involved particles are kaons, potential kaons are also discarded if they do not meet the correct criteria. Therefore, there is a loss of data for each applied PID cut. There are three different PID selections used throughout this analysis, which are as follows:

- No PID cuts.
- A TPC PID cut for kaons at $|\sigma_{kaon}| > 2$.
- A TPC PID cut for kaons at $|\sigma_{kaon}| > 2$ + A TOF PID veto for kaons at $|\sigma_{kaon}| > 3$.

The set without PID cuts will represent the raw minimum bias data, where M_{inv} is calculated for every particle pair, whether the track is a kaon or not. Although in such cases the statistics are large, the signal can not be resolved from the background throughout the lower (< 1.5 GeV/c) p_{T} region. The 2nd data set contains a kaon PID cut on the TPC detector (see Sec 3.1.2). $|\sigma_{kaon}| > 2$ signifies that, in the gaussian kaon $\mathrm{d}E/\mathrm{d}x$ distribution, every track outside of 2 σ Gaussian standard deviations (approximately 95.4% of the all identified kaons) of the kaon $\mathrm{d}E/\mathrm{d}x$ distribution is discarded. The last set requires the particle tracks to first pass the previous TPC cut, in addition to a PID veto on the TOF level (explained in Sec 3.1.3). The TOF veto is applied and keeps 3 $|\sigma|$ Gaussian standard deviations (approximately 99.7%) of the identified kaons. In this context, the term "veto" is used differently to what can be considered a cut; the veto requires the particle track to have a registered hit on the TOF detector, before the $3|\sigma|$ cut is applied. If the track does not have a registered TOF hit, no TOF cut is applied. When contrasted against each other, the three different sets will demonstrate how the systematical error alters due to the PID cuts.

Furthermore, kinematic cuts are applied in addition to the separate PID cuts. The kinematic cuts consist of a minimal p_{T} requirement of > 0.05 GeV, in addition with an acceptance cut on η, such that $|\eta| < 0.8$.

4.2.5 High Multiplicity & Spherocity Cuts

The ϕ yield from the four different (M_{inv}, p_{T}, ΔR)-distributions are further analyzed as functions of multiplicity and spherocity, for each PID set. The multiplicity and spherocity cuts are as follows:

- ϕ yield without any multiplicity or spherocity cuts.
- ϕ yield containing tracks from only high multiplicity events.
- ϕ yield containing tracks from only high multiplicity, low spherocity events.
- ϕ yield containing tracks from only high multiplicity, high spherocity events.

For the high multiplicity cut, the approximate multiplicity distribution is acquired by reconstructing the sum of the ionization signals from the V0 detector, and only 10% of the events that result in the largest signal are considered. The V0 signal spectrum, including the high multiplicity cut, is displayed in Fig 30. Similarly, the spherocity cuts are determined by reconstructing the S_0 distribution (requiring events to have at least 10 particle tracks), and only considering the events that are in the bottom/top 20% of the S_0 distribution, as seen in Fig 31.

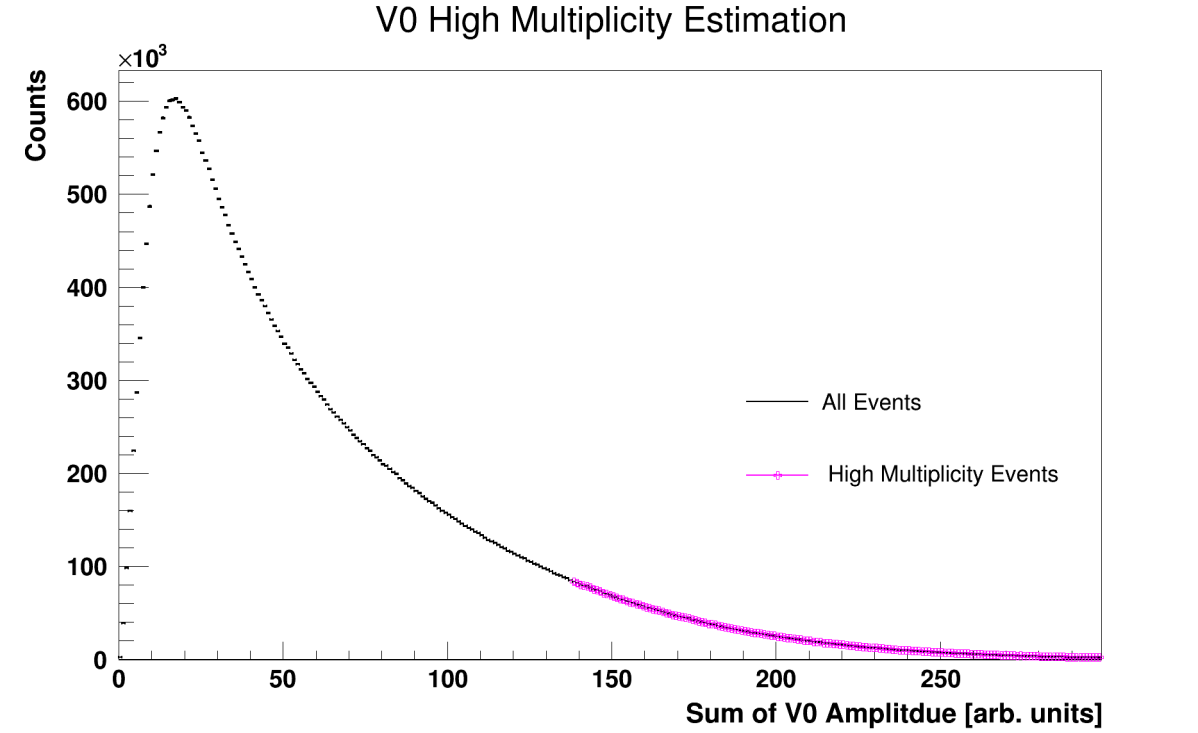

Figure 30: A V0M signal distribution for minimum bias p-p collisions at $\sqrt{s_{NN}} = 13$ TeV.

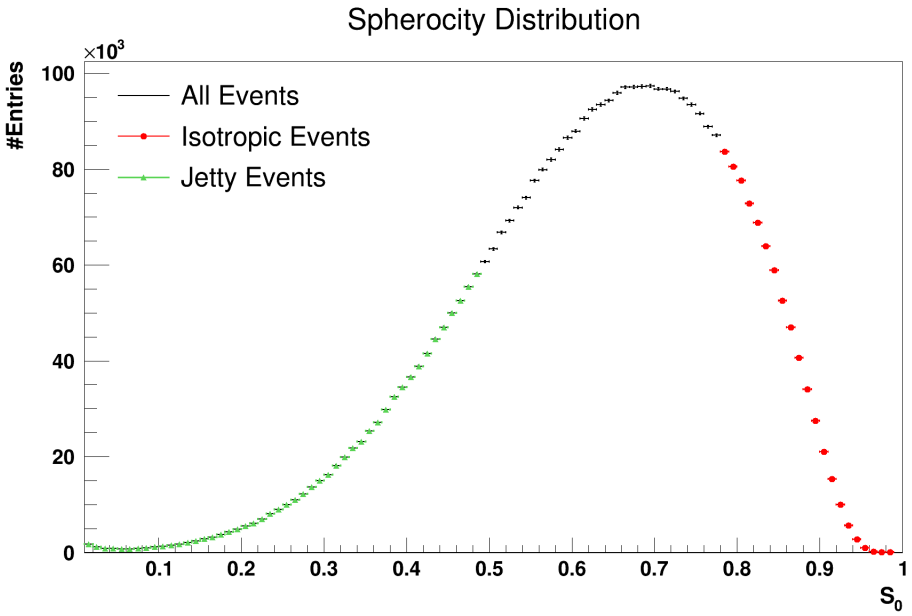

Figure 31: The spherocity distribution for the data in this analysis.

4.3 Efficiency Corrections

4.3.1 Simulated "Closure" Test

A 'closure' test was performed on reconstructed Monte Carlo (MC) simulated data, in order to gauge the performance of the analysis, as well as the systematic errors that arise due to the reweighed background.

As Monte-Carlo simulations label each particle with a specific particle label, it is therefore possible to reconstruct a "true" ϕ M_{inv} spectra, referred to as MC_{truth}, that only contains reconstructed ϕ particles. This is accomplished by making certain that the two kaons in the M_{inv} calculation belong to the same mother ϕ particle. This distribution will thereby only consist of a single peak, with a known integrated yield. The MC_{truth} distribution is then compared to a distribution that contains all reconstructed particle tracks, MC_{rec}. MC_{rec} will also contain the same phi peak as MC_{truth}, alongside a combinatorial background. The MC_{rec} distribution is run through the full analysis, and the output yield from the integrated BW function is compared to the integrated yield of MC_{truth}. An example of the MC_{truth} and MC_{rec} distributions for USSE, USME and rew. USME can be seen in Fig. 32, with a applied TPC cut + TOF veto, within the interval 2 GeV/c< p_T <4 GeV/c

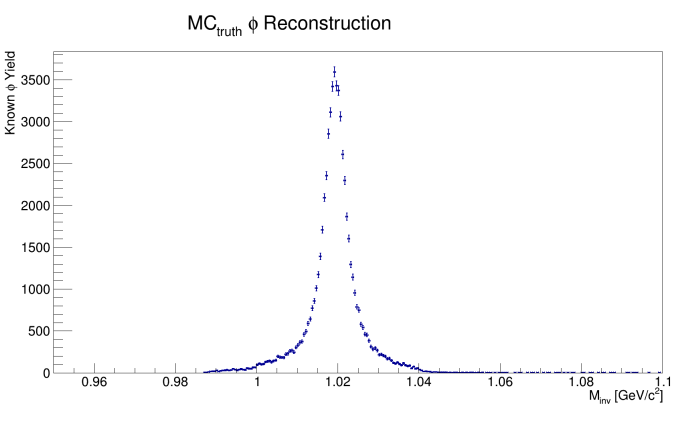

(a)

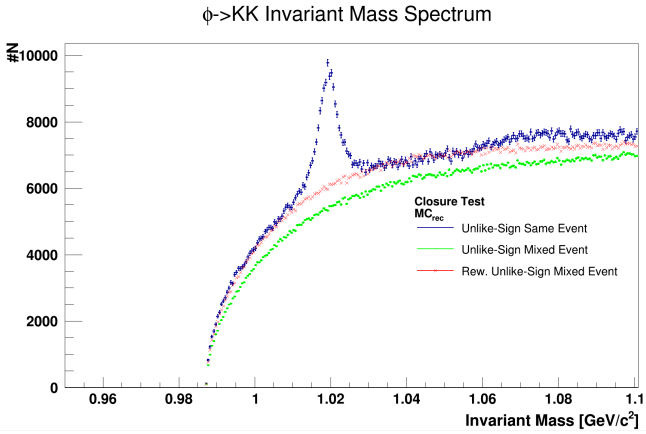

(b)

Figure 32: (a) The MC_{truth} M_{inv} signal distribution, within the interval 2 GeV/c< p_T <4 GeV/c. (b) The MC_{rec} M_{inv} signal distribution is compared to the USME and the reweighted USME background estimates,within the interval 2 GeV/c< p_T <4 GeV/c, see text for details.

4.3.2 Rapidity Correction

A rapidity correction is applied to the raw ϕ yield spectrum, in order to correct the discrepancy between pseudorapidity and rapidity at low p_{T}. The correction is performed by taking the following function:

$$\frac{y_{corr}(p_{\mathrm{T}})}{\eta} = \frac{\operatorname{arcsinh}\left(\frac{p_{\mathrm{T}}}{\sqrt{p_{\mathrm{T}}^2+M_\phi^2}}\sinh\eta\right)}{\eta}. \tag{20}$$

The rapidity correction can be seen plotted in Fig. 33 The raw ϕ yield spectrum is then individually corrected for each p_{T} bin, with the corresponding evaluated value in the rapidity correction.

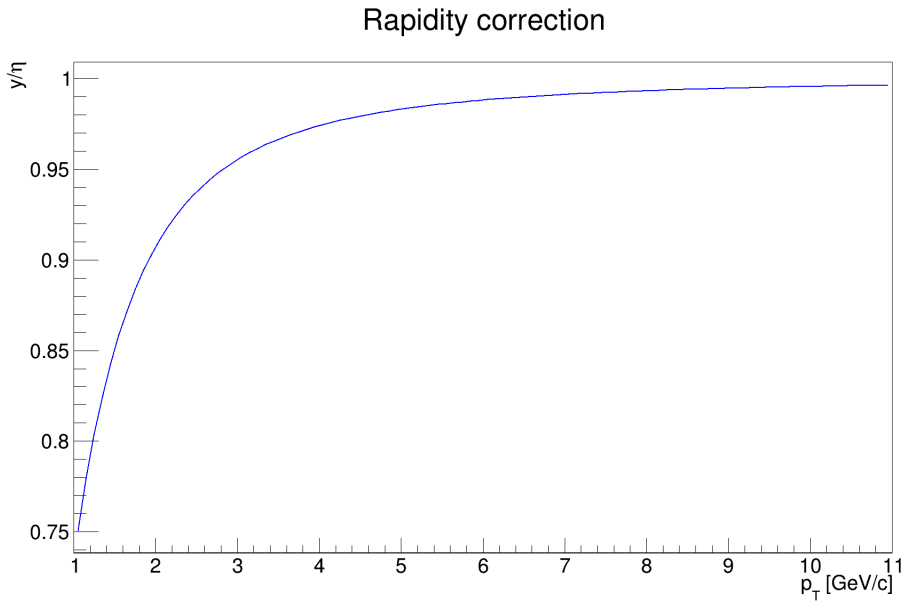

Figure 33: Rapidity correction plotted as a function of p_{T}

4.3.3 Detector Efficiency

A detectors ability to measure and record particles that are created during a collision is not perfect. The deficiency between reconstructed particles and actually 'created' particles is referred to as the detector efficiency. The detector efficiency accounts for particles that do not interact with the detector medium, as well as the detector's ability to convert particle tracks into useful signals.

The detector efficiency is calculated by using MC simulated data. The generated particles are transported through a simulation of the ALICE detector, using the same trigger conditions. The reconstructed output of the MC data is then compared to the initial input of the generated data, and the ratio between the input and the output is used as the detector efficiency. The efficiency is calculated for the same p_{T} intervals as the real analysis data, individually for every PID trigger set. These different distributions can be seen in Fig. 34, and the raw ϕ yield is then scaled accordingly in order to correct for the detector efficiency.

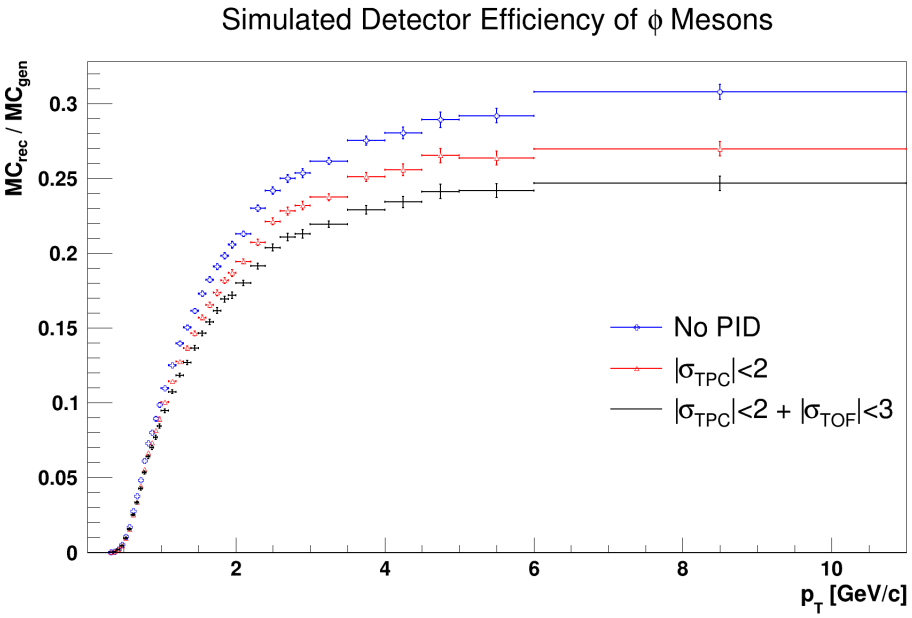

Figure 34: Distributions of detector efficiencies for the various PID cuts.

5 Results & Discussion

5.1 Run Statistics

Table 1: A table presenting the total amount of events for the different multiplicity and spherocity bins

	#Events	#Events after Vrtx. Corr	% of OK Vrtx's	% of MB Events
Minimum Bias	4.25419e+07	4.33709e+07	0.965672	N/A
High Multiplicity	4.24441e+06	4.24441e+06	1.00	0.099770
Jetty High Multiplicity	814224	814224	1.00	0.019139
Iso. High Multiplicity	824536	824536	1.00	0.019138

The number of particles contained in each multiplicity and spherocity selection can be seen in Table 1. The vertex correction discards the events where no reconstructed vertex was found. It can be seen that the statistics for the high multiplicity distributions, and even more so the different spherocity limits, are limited compared to the minimum bias data. Thus, the ϕ yield for the high multiplicity distributions will need to be measured over larger p_{T} intervals in order to have a reasonable yield extraction.

5.2 Closure Test

To evaluate the precision of the signal extraction a closure test was applied to MC simulated data. The advantage with MC data is that one knows the true number of ϕ particles, see Fig. 32(b). The results from the closure test, seen in Table 2, show that the integrated BW fit and the background fit was evaluated correctly from the corresponding distributions seen in Fig. 32. As both the non-reweighed and reweighed USME distributions had the same fitting parameters, and knowing the correct number of ϕ particles from the simulation, Table 2 also shows that the integrated ϕ yield overestimates the number of ϕ particles for the mid-range p_{T}, whereas the ϕ yield gained using the reweighing background reduction slightly underestimates the number of ϕ particles. However, both methods behave similarly for the other low and high p_{T} intervals.

Table 2: A table containing the results from the MC_{rec} closure test. Errors shown are purely statistical

	ϕ Yield	MC_{truth} / MC_{rec}
1 GeV/c < p_T <2 GeV/c		
MC_{truth} ϕ yield	93550±305.859	N/A
MC_{rec} ϕyield	93324±305.491	1.003
Rew. MC_{rec} ϕ yield	93131±305.173	1.004
2 GeV/c < p_T <4 GeV/c		
MC_{truth} ϕ yield	61310±247.609	N/A
MC_{rec} ϕyield	67739±260.267	0.905
Rew. MC_{rec} ϕ yield	60434±245.833	1.014
4 GeV/c < p_T <11 GeV/c		
MC_{truth} ϕ yield	11640±107.889	N/A
MC_{rec} ϕyield	11887±109.027	0.979
Rew. MC_{rec} ϕ yield	12010±109.585	0.970

5.3 M_{inv} Distributions Across Different p_T ranges.

The USSE, USME and reweighed USME M_{inv} distributions, across different p_T bins, for different PID selections, can be seen through Fig. 35 - 43. The reweighed distributions were all reweighed in the M_{inv} range of 0.95-1.35 GeV/c, but normalized to the region between 1.15 GeV/c < M_{inv} < 1.20 GeV/c. One can note that the overall shape of the peak and background depends heavily on the selected p_T range, as well as the given PID cut. This is due to other interfering particles, such as π mesons and protons, that gradually disappear for larger values of p_T, as well as with each applied PID cut. Likewise, it is seen that the performance of the reweighing process depends on the p_T range. As p_T increases, so does the probability that the tracks used in the M_{inv} calculation originated from jets. The value of ΔR is thus sensitive to the selected p_T interval.

Comparing the distributions with different PID cuts, but within the same p_T intervals (Fig. 35 to Fig. 38 and Fig. 41, etc), one can note that the reweighing follows the same trend within each p_T interval. For the low p_T region, the reweighed background goes under the signal distribution at the far end of the spectrum, the mid p_T region fits the whole signal distribution tightly, and the reweighed background distribution overshoots over the signal distribution in the high p_T limit. This phenomenon could again be due to that the variation of the average geometric path, for the available tracks, becomes restricted towards larger values of p_T. The reason for this behavior could also be due to the correlated background within the signal distribution. The signal is barely resolvable in Fig. 31, and there is a distinguished 2nd "bump" visible in Fig. 36 - 39, as well as in Fig. 42 , around 1.05 GeV/c < M_{inv} < 1.1 GeV/c. This bump is due to K^0_s particles, a weaker eigenstate of the kaon, being produced in the collision, which will decay into π^+ π^- pairs. At low p_T, it has been shown by collaborators in ALICE that this will give rise to such a peak if we cannot reject the pions. This bump is thus visible, as each particle track has to be considered a kaon for the M_{inv} calculation (as explained in Sec 4.2). This correlation, as well as other correlated effects, can not be reproduced in the mixed-event background distribution. Furthermore, it can be seen that the K^0_s, particles diminish with each applied PID cut, as does the pronunciation of the defect from the reweighed background at the end of the spectrum.

However, throughout all of the presented p_T intervals, the reweighed background distribution performs better than the non-reweighed background distribution around the signal peak. This allows for a much cleaner signal extraction, and the following signal and background fits will not have to be as complex in order to fit and describe the data. This can clearly be seen in the ϕ signal extractions for the TPC+TOF distributions. The distributions in this case have almost a linear background, where the task to fit signal becomes a simple task, whereas the signal extraction in cases such as shown in Fig. 35 proves to be non-trivial.

5.3.1 M_{inv} With No PID Cuts

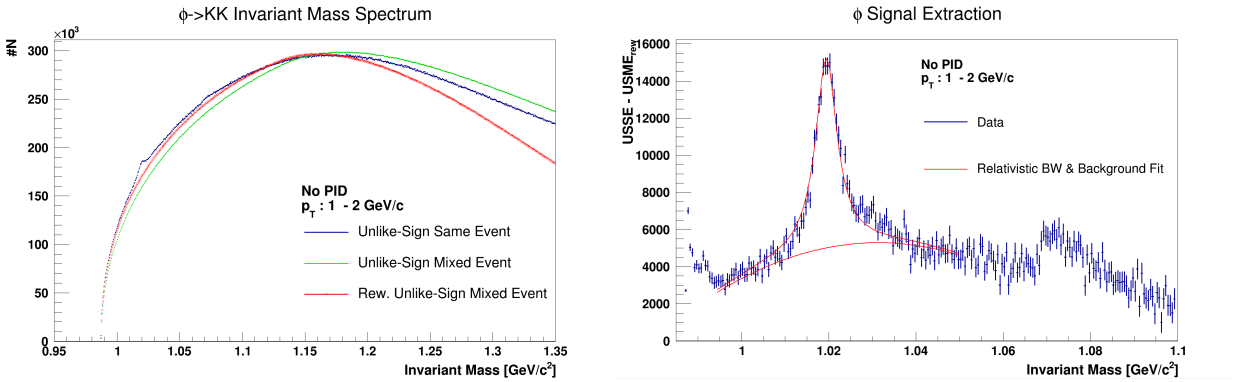

(a) (b)

Figure 35: a) M_{inv} spectra of USSE, USME & reweighed USME distributions, with no PID cuts, in the 1 GeV/c $< p_{\mathrm{T}} <$ 2 GeV/c GeV/c interval, normalized to $1.15 < M_{inv} < 1.20$. b) The extracted and fitted USSE - reweighed USME ϕ yield in the 1 GeV/c $< p_{\mathrm{T}} <$ 2 GeV/c interval, with no PID cuts.

,

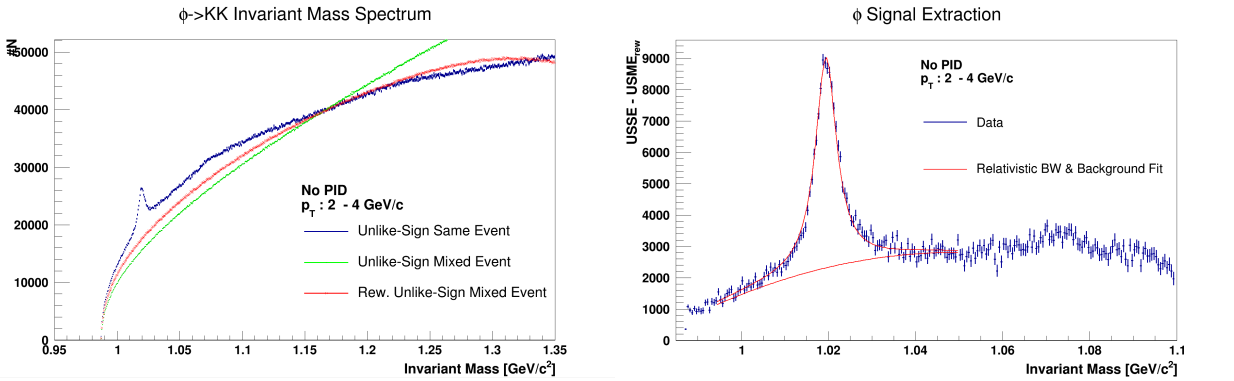

(a) (b)

Figure 36: a) M_{inv} spectra of USSE, USME & reweighed USME distributions, with no PID cuts, in the 2 GeV/c $< p_{\mathrm{T}} <$ 4 GeV/c interval, normalized to $1.15 < M_{inv} < 1.20$. b) The extracted and fitted USSE - reweighed USME ϕ yield in the 2 GeV/c $< p_{\mathrm{T}} <$ 4 GeV/c interval, with no PID cuts.

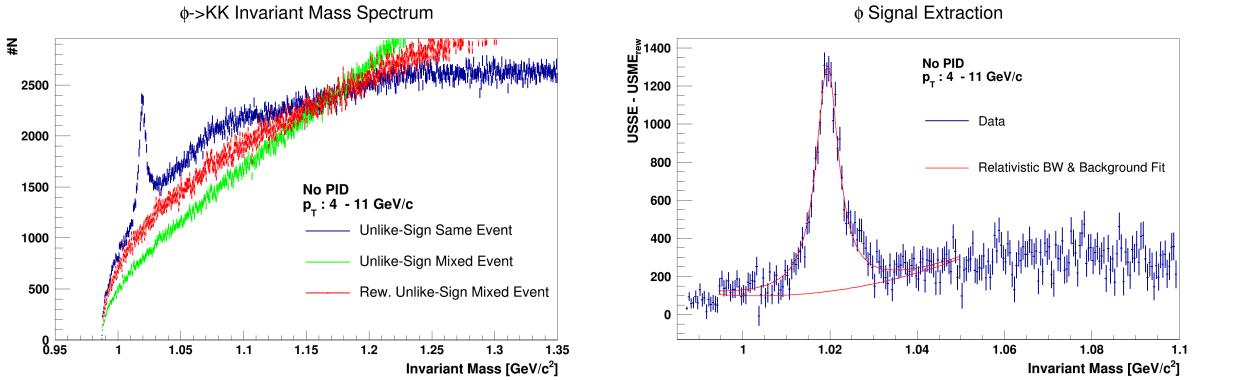

(a) (b)

Figure 37: a) M_{inv} spectra of USSE, USME & reweighed USME distributions, with no PID cuts, in the 4 GeV/c $< p_{\mathrm{T}} <$ 11 GeV/c interval, normalized to $1.15 < M_{inv} < 1.20$. b) The extracted and fitted USSE - reweighed USME ϕ yield in the 4 GeV/c $< p_{\mathrm{T}} <$ 11 GeV/c interval, with no PID cuts.

5.3.2 M_{inv} With a TPC Cut

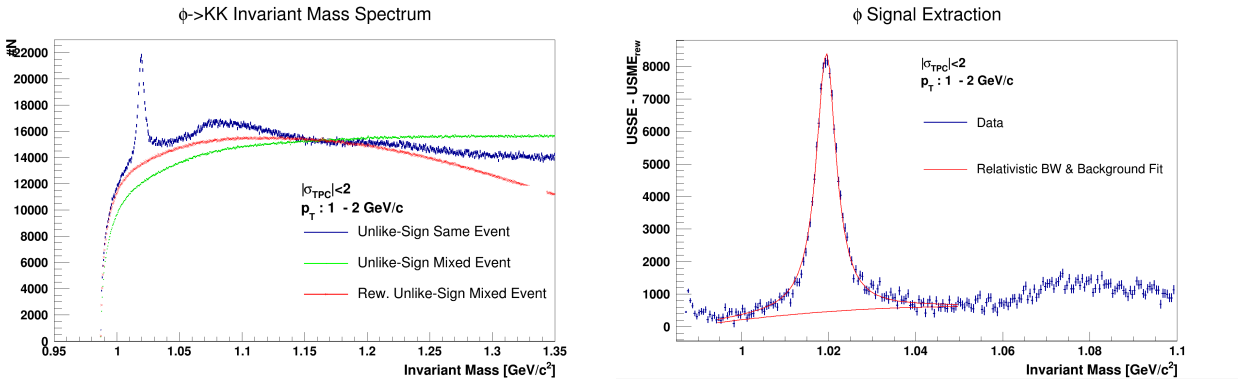

(a) (b)

Figure 38: a) M_{inv} spectra of USSE, USME & reweighed USME distributions, with a TPC PID cut, in the 1 GeV/c $< p_{\mathrm{T}} <$ 2 GeV/c interval, normalized to $1.15 < M_{inv} < 1.20$. b) The extracted and fitted USSE - reweighed USME ϕ yield in the 1 GeV/c $< p_{\mathrm{T}} <$ 2 GeV/c interval, with a TPC PID cut.

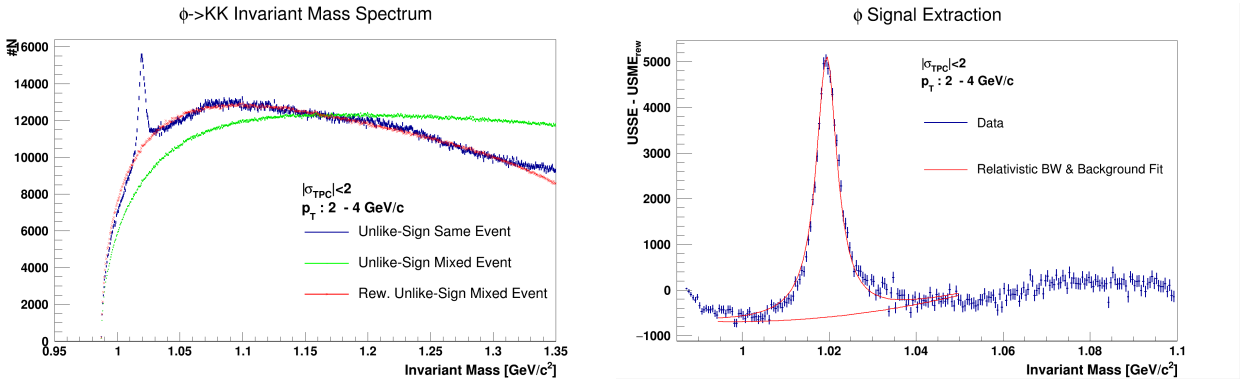

(a) (b)

Figure 39: a) M_{inv} spectra of USSE, USME & reweighed USME distributions, with a TPC PID cut, in the 2 GeV/c $< p_{\mathrm{T}} <$ 4 GeV/c interval, normalized to $1.15 < M_{inv} < 1.20$. b) The extracted and fitted USSE - reweighed USME ϕ yield in the 2 GeV/c $< p_{\mathrm{T}} <$ 4 GeV/c interval, with a TPC PID cut.

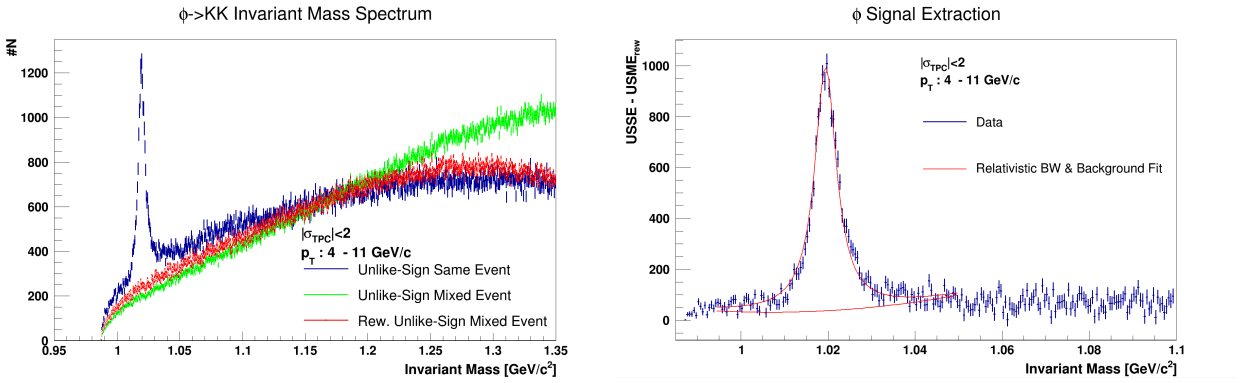

(a) (b)

Figure 40: a) M_{inv} spectra of USSE, USME & reweighed USME distributions, with a TPC PID cut, in the 4 GeV/c $< p_{\mathrm{T}} <$ 11 GeV/c interval, normalized to $1.15 < M_{inv} < 1.20$. b) The extracted and fitted USSE - reweighed USME ϕ yield in the 4 GeV/c $< p_{\mathrm{T}} <$ 11 GeV/c interval, with a TPC PID cut.

5.3.3 M_{inv} With a TPC Cut + TOF veto

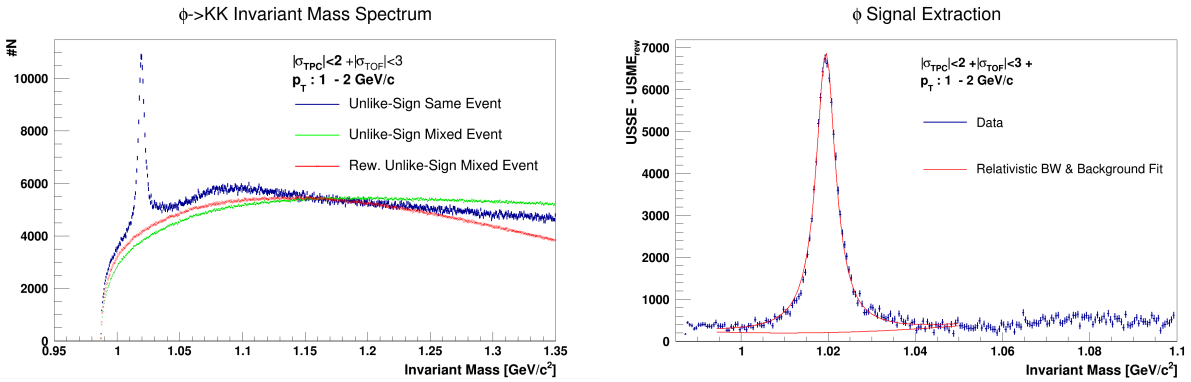

(a) (b)

Figure 41: a) M_{inv} spectra of USSE, USME & rew. USME distributions, with a TPC PID cut + TOF veto, in the 1 GeV/c $< p_{\mathrm{T}} <$ 2 GeV/c interval, normalized to $1.15 < M_{inv} < 1.20$. b) The extracted USSE - rew. USME ϕ yield in the 1 GeV/c $< p_{\mathrm{T}} <$ 2 GeV/c interval, with a TPC PID cut + TOF veto.

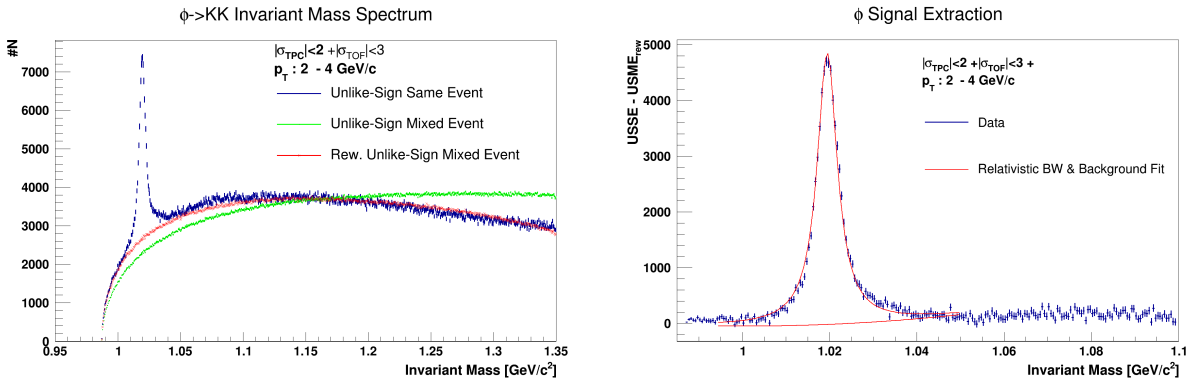

(a) (b)

Figure 42: a) M_{inv} spectra of USSE, USME & rew. USME distributions, with a TPC PID cut + TOF veto, in the 2 GeV/c $< p_{\mathrm{T}} <$ 4 GeV/c interval, normalized to $1.15 < M_{inv} < 1.20$. b) The extracted USSE - rew. USME ϕ yield in the 2 GeV/c $< p_{\mathrm{T}} <$ 4 GeV/c interval, with a TPC PID cut + TOF veto

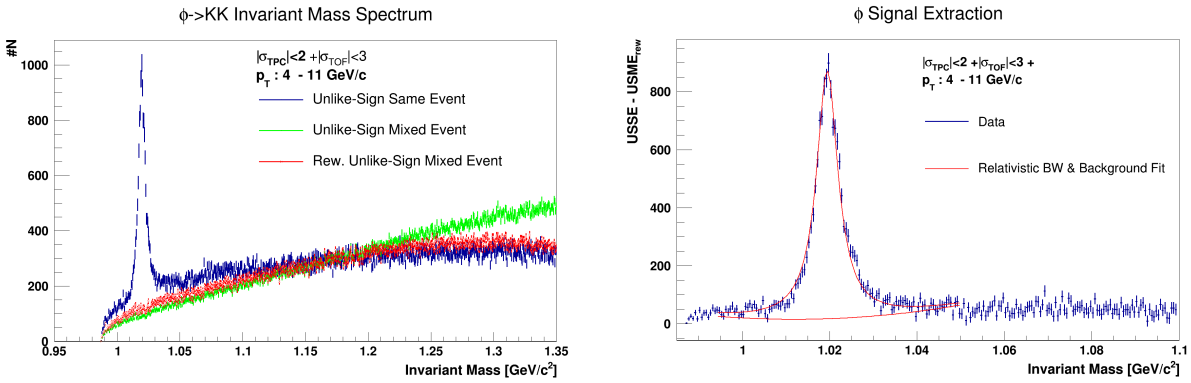

(a) (b)

Figure 43: a) M_{inv} spectra of USSE, USME & rew. USME distributions, with a TPC PID cut + TOF veto, in the 4 GeV/c $< p_{\mathrm{T}} <$ 11 GeV/c interval, normalized to $1.15 < M_{inv} < 1.20$. b) The extracted USSE - rew. USME ϕ yield in the 4 GeV/c $< p_{\mathrm{T}} <$ 11 GeV/c interval, with a TPC PID cut + TOF veto

5.4 Corrected ϕ Yield

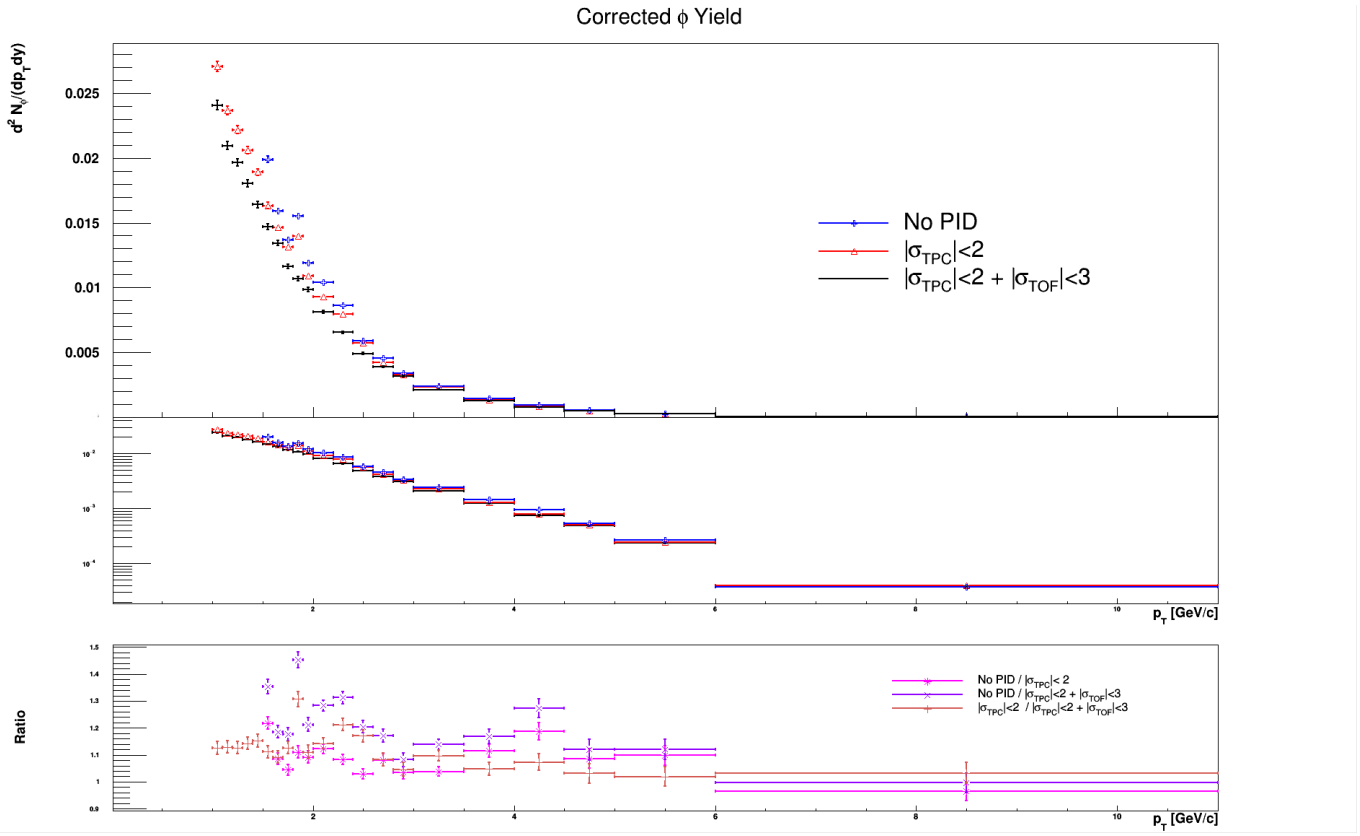

Figure 44: Corrected ϕ yield, with ratios between PID cuts, presented in both a linear and logarithmic scale.

The corrected (vertex, efficiency & rapidity corrections) ϕ yield can be seen in Fig. 44. One can note that the non-PID spectrum in Fig. 44 does not have any values in the range of $p_{\mathrm{T}} < 1.15$ GeV/c, while the other distributions do. The reason for this becomes apparent when comparing Fig. 35 to Fig. 38 and Fig 41. The peak resolution for the non-PID spectra is barely sufficient in a single 1.0 GeV/c - 2 GeV/c p_{T} bin, and completely disappears if the bin is reduced further. However, the ϕ yields of each of the distributions were still measured in the low p_{T} region, as they do have resolvable signal peaks there (as can be seen in Fig. 38 and Fig. 41). These measurements are important, as it is in the low p_{T} region where strangeness production cannot be calculated through perturbative QCD methods.

As can be seen in Fig. 44 , the total amount of measured ϕ mesons decreases with each applied PID cut. However, the disparity between each distribution decreases with increasing p_{T}. This is in agreement of what is seen in Fig. 35 - 43. As p_{T} increases, the correlated background within the USSE distributions becomes increasingly comparable. The difference between the PID cuts in Fig. 44 could either be due to potential ϕ particles being discarded for not meeting the PID criteria, or that the signal extraction is overestimated (contains background) for the No PID and TPC cut spectra. An attempt to investigate this can be seen in Fig. 45, which displays ratios in efficiency and raw data between the non-discriminated and discriminated distributions. It can be seen that the difference in efficiency between the TPC cut and the TPC cut + TOF veto is not solely enough in order to describe the difference seen in the raw data. If that was the case, the amplitude between the efficiency ratio would be the same as the amplitude between the data ratio, in each p_{T} bin. As is seen in the figure, this is not the case, heavily pronounced so at the lower p_{T} region, and gradually becoming better as p_{T} increases. As such, the difference between the two sets of PID cuts is either due to a combination of both underestimation of background and lost ϕ particles due to the PID criteria, or the calculated efficiency correction is inadequate to describe the difference in efficiency for each applied PID cut.

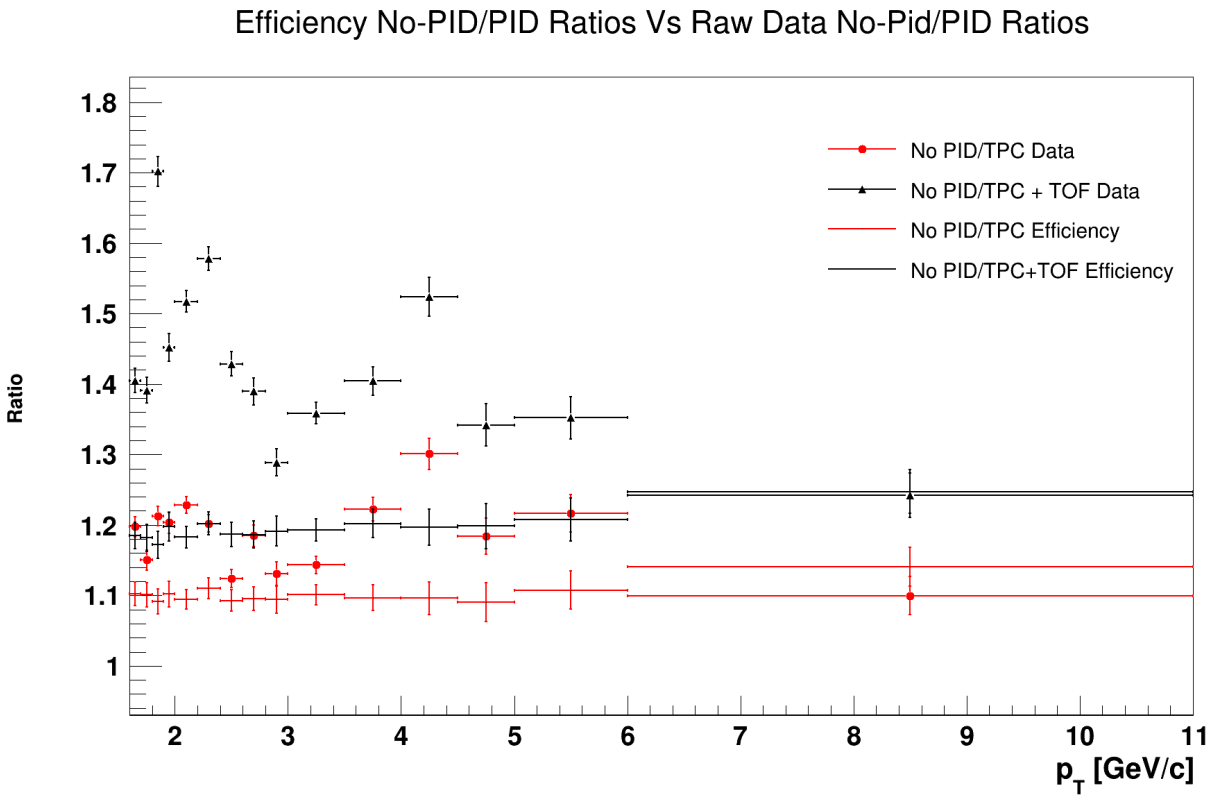

Figure 45: Ratios between non-discriminated and discriminated of efficiency and raw data.

5.5 ϕ Yield Across Different Spherocities & Multiplicities

As there seem to be some apparent issues with the detector efficiency for the different PID selections, as seen in Fig. 45, all three different PID cuts will be kept throughout the remainder of the analysis. A comparison between the individual distributions from Fig. 44 and their high multiplicity & low/high spherocity counterparts can be seen through Fig. 46 - 48.

Keep in mind that the, in this context, term 'minimum bias' refers to the lack of any spherocity and multiplicity cuts, and not the PID different selections. As can be seen through the figures, the ϕ yield is enhanced for all three high multiplicity distributions as compared to the minimum bias distributions, for each PID selection. One can also note a novel feature where the ϕ yield from the jetty distribution crosses with the ϕ yield from the isotropic distribution around $p_{\mathrm{T}} \approx 3$ GeV/c. This is as expected, due to the nature of how S_0 is defined. Since a smaller p_{T} is characteristic to isotropic events, and events containing larger p_{T} tracks tend to be more jetty. While the figures show an enhancement of ϕ mesons in the high multiplicity distribution compared to the minimum bias distributions, it is not enough to justify an enhancement of strange particles, as the nature of large multiplicity events induces an overall enhancement of all particle production.

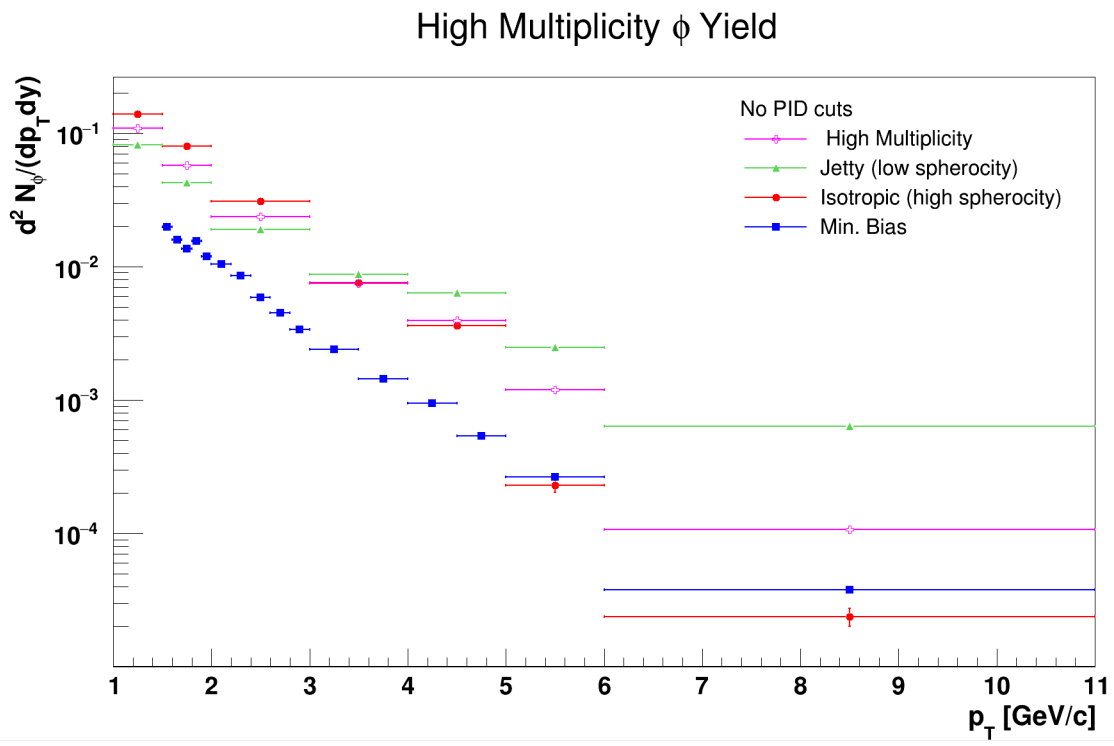

Figure 46: Corrected ϕ yield, measured with no PID cut, with high multiplicity and spherocity cuts, normalized accordingly to the number of events in each case, across p_{T}.

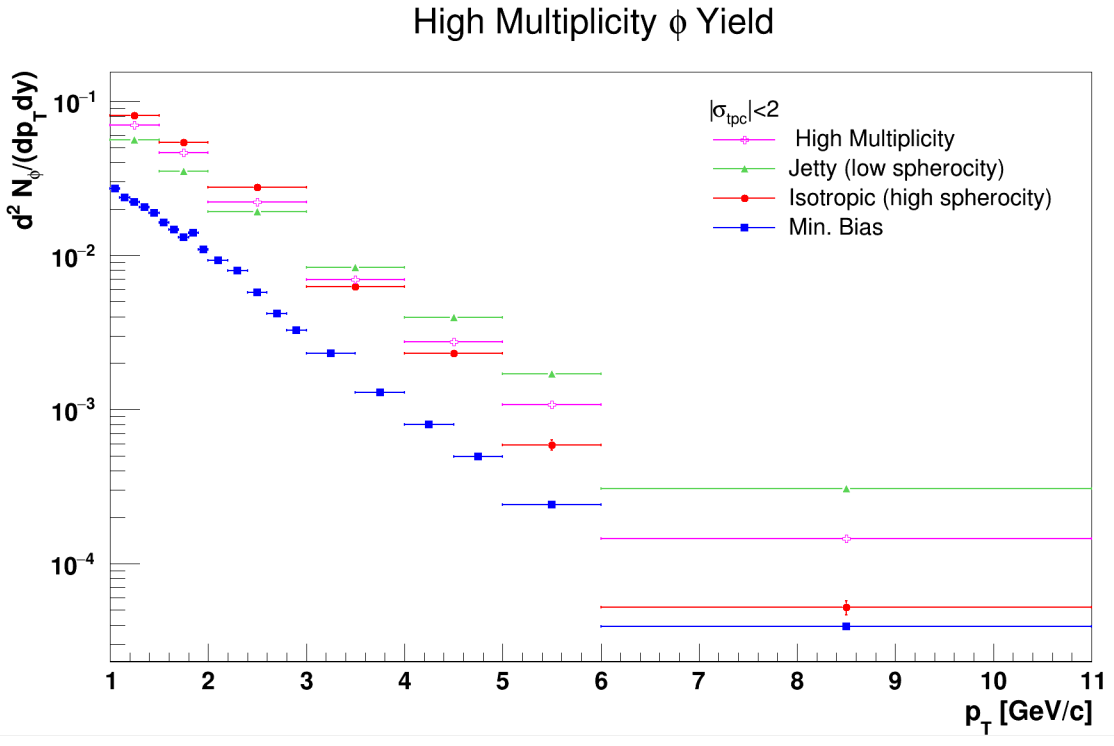

Figure 47: Corrected ϕ yield, measured with a TPC cut, with high multiplicity and spherocity cuts, normalized accordingly to the number of events in each case, across p_{T}.

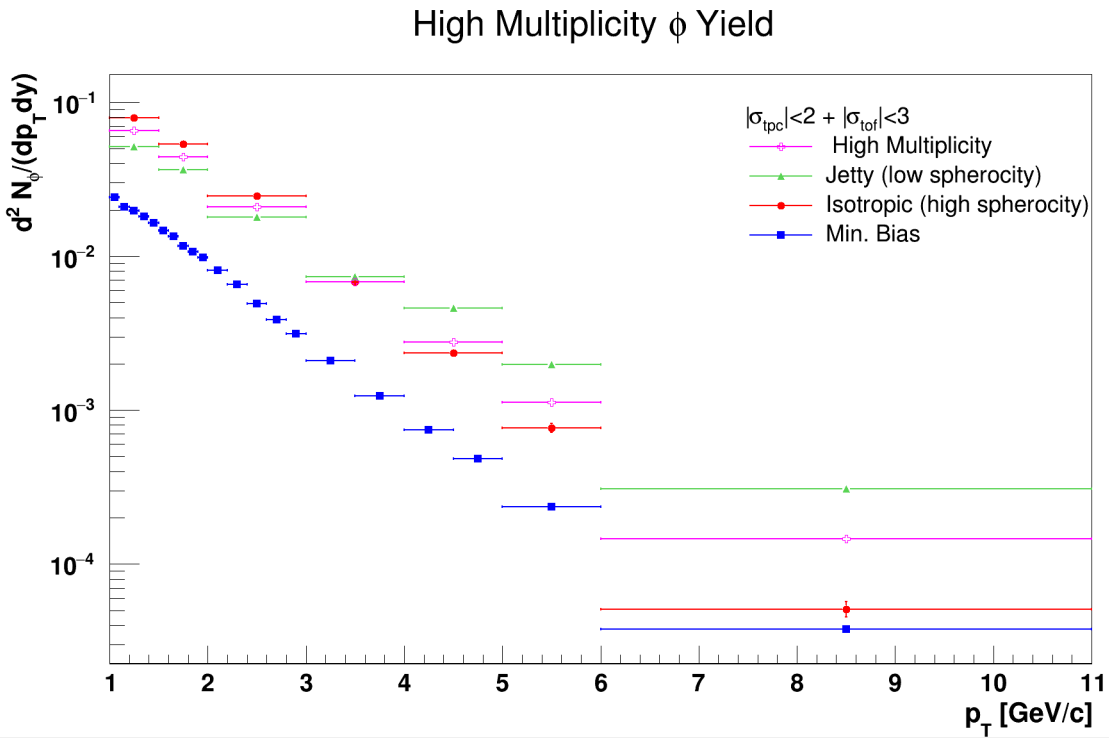

Figure 48: Corrected ϕ yield, measured with a TPC cut and a TOF veto, with high multiplicity and spherocity cuts, normalized accordingly to the number of events in each case, across p_{T}.

5.6 ϕ / $N_{charged}$

In order to gauge whether the high multiplicity events have an enhanced strangeness production compared to minimum bias events, the fraction of measured ϕ mesons versus the overall measurement of charged particles, $N_{charged}$, has to be sufficiently larger in the high multiplicity event sample, than in the minimum bias event sample. Ratios between the ϕ yield and $N_{charged}$ for each multiplicity and spherocity cut are displayed throughout Fig. 49 - 51, each with a different PID criteria. It can be seen throughout the figures that there is a general enhancement of ϕ particles in the high multiplicity distributions compared to the minimum bias distribution, independent of the PID cuts. These results agree with the results from the recent study on strangeness production in p-p collisions presented in Section 2.6, which noted an enhancement of the multistrange (containing more than 1 strange quark) Λ and Ω particles.

A novel feature is exhibited throughout Fig. 49 - 51, which is that there is also a pronounced enhancement of measured ϕ particle production in the isotropic, low spherocity events, compared to the jetty, high spherocity events. This is interesting, as it can be seen that the jetty and minimum bias distributions exhibit similar behavior. This supports that the strangeness production in minimum bias events is most likely dominated by hard processes that occur during jetty collisions, which was already expected from the Lund-String Model. On the other hand, if only the high multiplicity distributions are considered, it becomes apparent that the ϕ production in high multiplicity events is dominated by isotropic events, most likely through soft processes. The difference in enhancement between the isotropic and jetty distributions almost reaches 50%, in some p_{T} intervals (what could perhaps be considered as 'super-enhancement'). Furthermore, if ϕ production would follow a string-like model, one would expect that the jetty events would be the main contributing factor for the ϕ enhancement in high multiplicity events, due to the idea that more jetty collisions should lead to a larger amount of string breakings, and thus a larger amount of ϕ particles. However, the ϕ enhancement in high multiplicity seem to be dominated by isotropic events rather than jetty events, which is what one would expect if the ϕ production was due to a QGP-phase, described by a statistical model.

Compared to the study on simulated particle production using PYTHIA, as discussed in Sec. 2.7.5, the results between this study and the aforementioned one are in some agreement. While both Fig. 14 and Fig. 49 - 51 show an enhanced production of ϕ mesons in isotropic events compared to jetty events, the distributions do not quite look the same. The simulated isotropic distribution of the ϕ yield compared to the π yield in Fig.14 keeps increasing with p_{T}, whereas, as seen in Fig. 49 - 51 the ϕ distribution dips

back down around 5 GeV/c $< p_{\mathrm{T}} <$ 11 GeV/c.

As seen in Fig. 49, the distribution of the two last p_{T} bins with no PID cuts behaves differently compared to the distributions with an applied PID cut, Fig. 50 and Fig. 51, where the isotropic distributions drop to a significantly smaller value, even below the jetty distribution. Further insight into this issue can be seen below in Fig. 52 - 54, where the isotropic and jetty M_{inv} distributions, as well as their corresponding ϕ signal extraction, are compared between different PID cuts in the p_{T} interval under question. It can be seen in Fig. 52 (b), for the case with no PID cut, that the ϕ signal is almost unintelligible after the background reduction, even though there is a small hint of a signal peak in Fig.52 (a).

Comparing Fig.52 to the isotropic distribution with an applied TPC cut + TOF veto, displayed in Fig. 53, yield a intelligible signal resolution, although containing a smaller amount of total statistics. This is most likely due to a inherent problem with the reweighing method for the background subtraction, rather than solely due to the lack of statistics. This can already be seen in the minimum bias distributions with different PID selections, in Fig. 37 and Fig. 43. The reweighed background distribution without a PID cut performs worse than the distribution with a PID cut. The reason why this impacts the isotropic distribution more than the other ones in Fig. 49, is due the small amount of tracks with a large p_{T} from events with a large spherocity. As seen in Fig. 54, the same inherent defect from the reweighed background is still there for the jetty distribution, but the peak is still resolvable due to the amount of statistics.

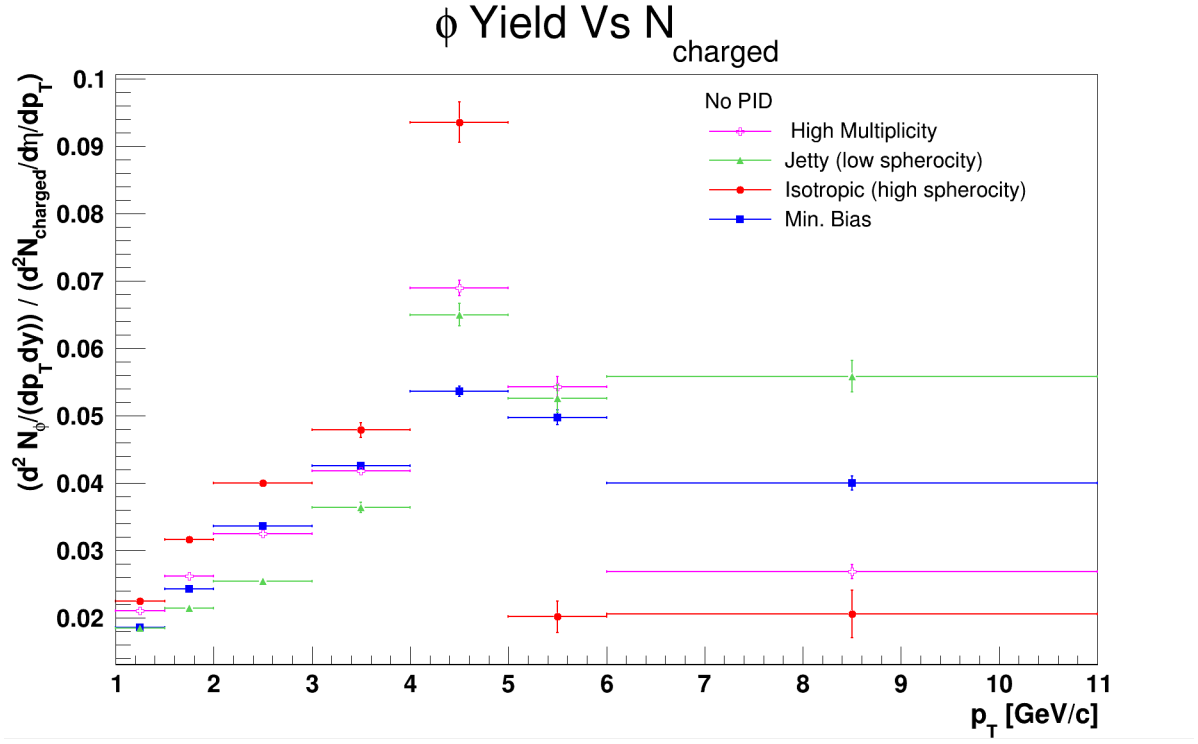

Figure 49: Corrected ϕ yield, measured with no PID cuts, with high multiplicity and spherocity cuts, normalized accordingly to the number of events in each case, across p_{T}.

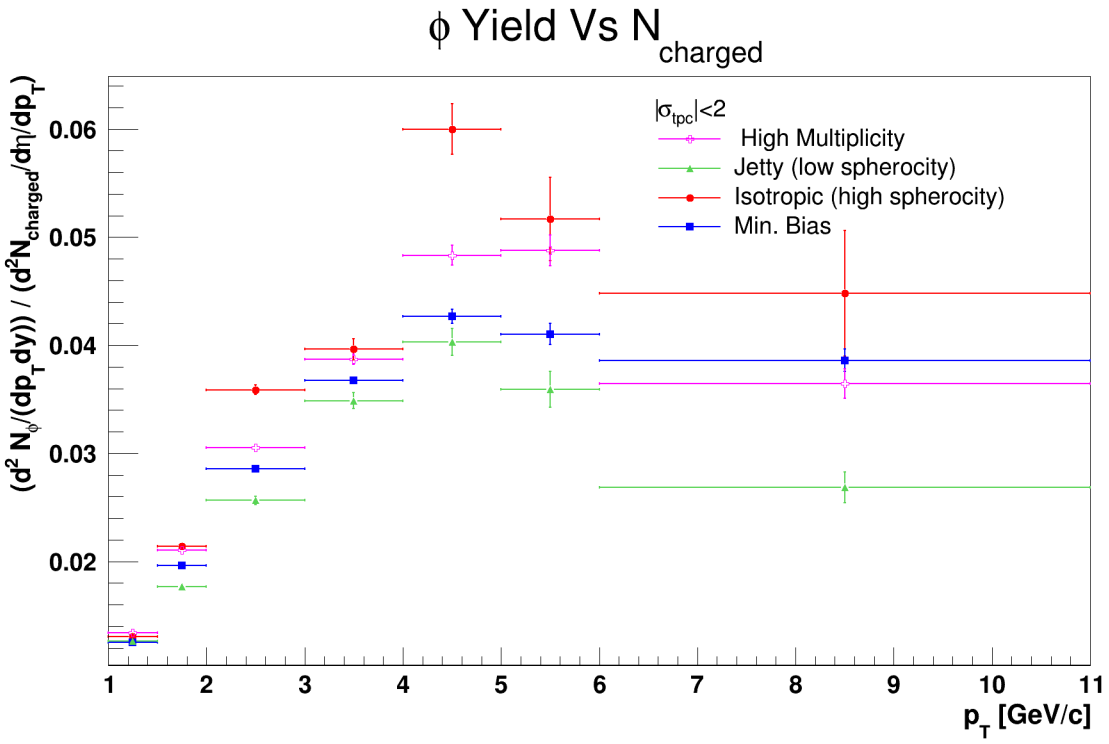

Figure 50: Corrected ϕ yield, measured with a TPC cut, with high multiplicity and spherocity cuts, normalized accordingly to the number of events in each case, across p_{T}.

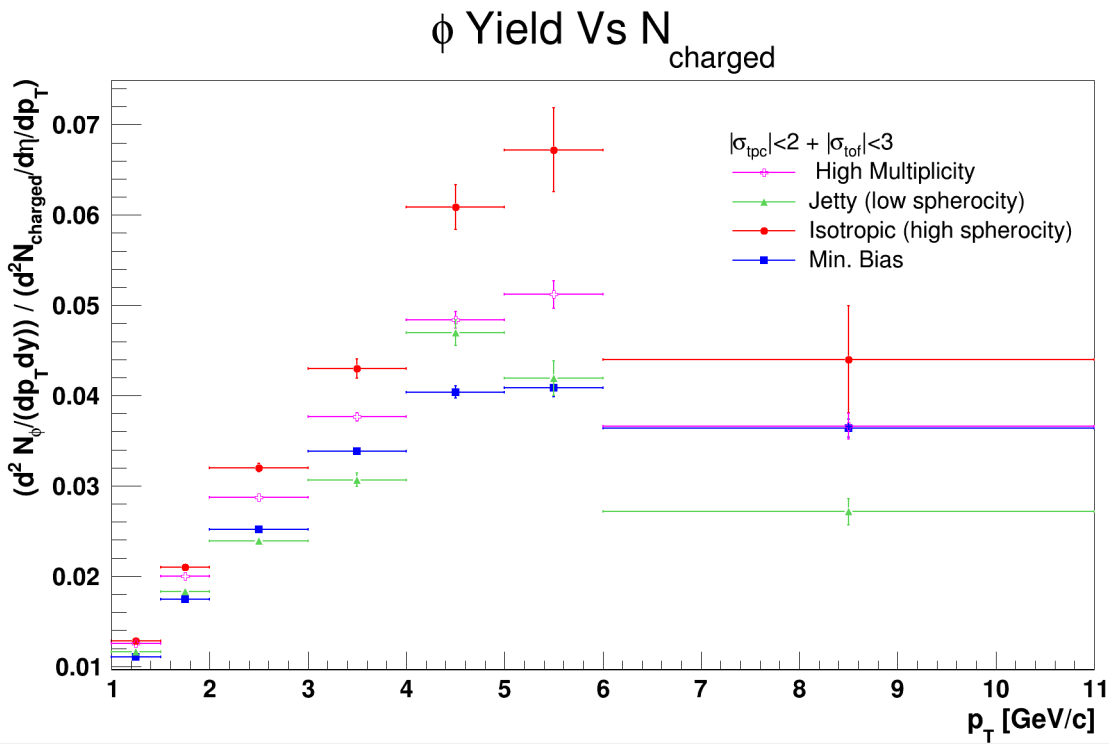

Figure 51: Corrected ϕ yield, measured with a TPC cut and TOF Veto, with high multiplicity and spherocity cuts, normalized accordingly to the number of events in each case, across p_{T}.

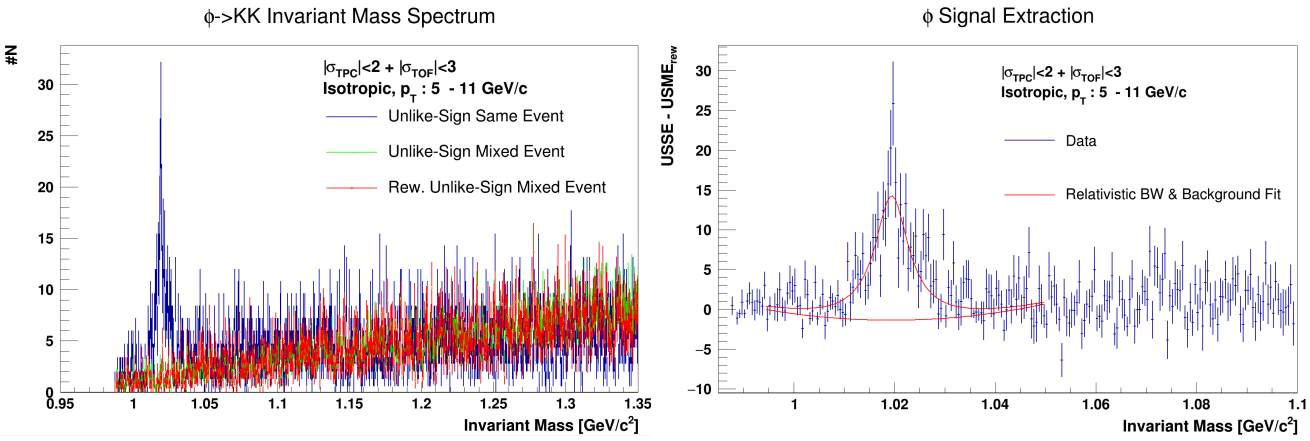

(a) (b)

Figure 52: a) A figure displaying the USSE, USME & rew. USME M_{inv} distributions for high multiplicity isotropic events, with a TPC cut + TOF veto, within the 5 GeV/c $< p_{\mathrm{T}} <$ 11 GeV/c interval. b) The ϕ signal extraction for high multiplicity isotropic events, with a TPC cut + TOF veto, within the 5 GeV/c $< p_{\mathrm{T}} <$ 11 GeV/c interval.

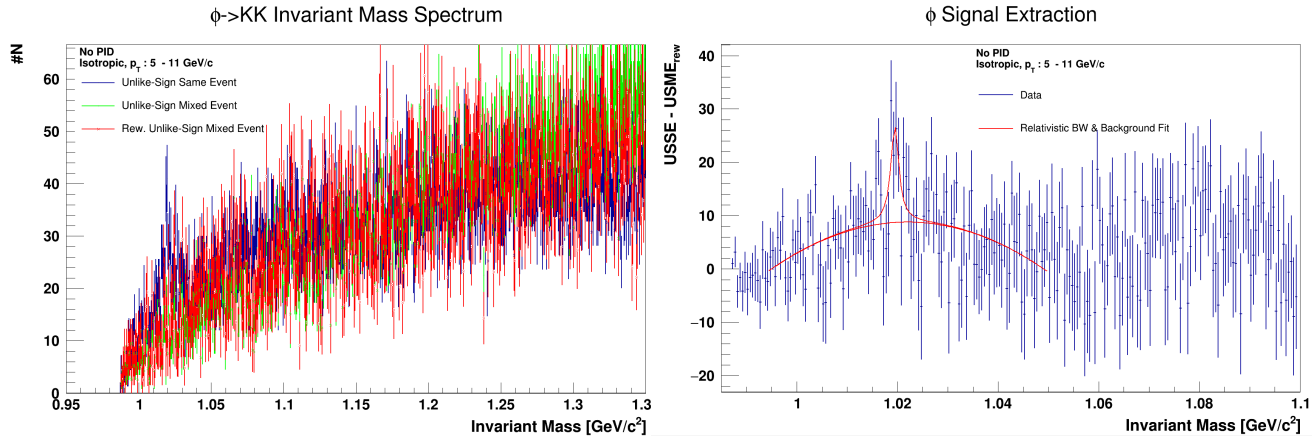

(a) (b)

Figure 53: a A figure displaying the USSE, USME & rew. USME M_{inv} distributions for high multiplicity isotropic events, without PID cuts, within the 5 GeV/c $< p_{\mathrm{T}} <$ 11 GeV/c interval. b) The ϕ signal extraction for high multiplicity isotropic events, without PID cuts, within the 5 GeV/c $< p_{\mathrm{T}} <$ 11 GeV/c.

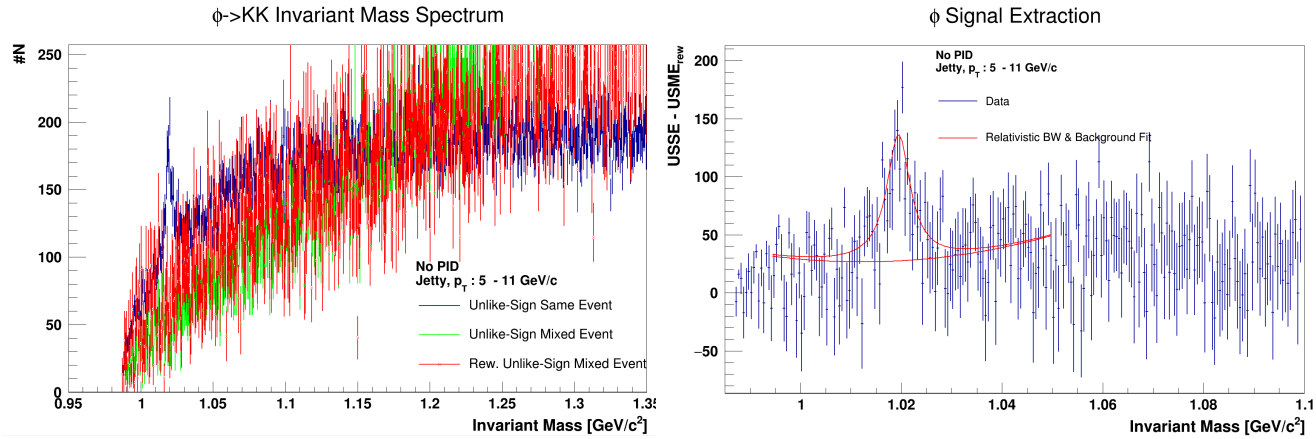

(a) (b)

Figure 54: a) A figure displaying the USSE, USME & rew. USME M_{inv} distributions for high multiplicity jetty events, without PID cuts, within the 5 GeV/c $< p_{\mathrm{T}} <$ 11 GeV/c interval. b) The ϕ signal extraction for high multiplicity jetty events, without PID cuts, within the 5 GeV/c $< p_{\mathrm{T}} <$ 11 GeV/c interval.

6 Conclusion & Outlook

In conclusion, Fig. 35 through Fig. 43 show that the reweighing method overall performs well for subtracting the background from the ϕ signal peak, across the different PID selections. However, there are some aspects of the reweighing that are perhaps not perfectly understood, as can be seen in the high p_{T} region for the distribution without a PID cut. Further investigation into how the reweighing process performs, with a larger selection of PID cuts, could thus be necessary.

A clear enhancement of ϕ particles can be seen in high multiplicity p-p collisions, where the enhancement is dominated by events with an isotropic distribution rather than a jetty distribution. This might indicate that the Lund-String like models are inadequate at describing the strangeness enhancement, and that the strangeness enhancement perhaps could be better explained by a statistical hydrodynamic model. While the results does not necessarily prove that a QGP-phase was created or not, it is certain that p-p collisions at high multiplicities are not currently well described. The new, soft physics described by the super-enhancement in the isotropic high multiplicity spectra is not yet well understood, and requires more studies in a similar vein. More thorough studies into the production of strange particles at high multiplicity p-p collisions, both how such collisions are produced in PYTHIA, as well as how they are produced in real data, are required, with the prospect of gaining a microscopic understanding of strangeness production.

It is important to note that the efficiency corrections used between the different high multiplicity & spherocity cuts remain constant. The difference in efficiency corrections only accounts for the applied PID cuts. Whether the efficiency drastically alters between multiplicity & spherocity cuts should be examined for further studies. It is also worth to consider whether the efficiency for the ϕ can be factorized by individual efficiencies for K^+ and K^-, in order to better understand the underlying detector efficiency for the ϕ meson with different PID selections. What was not performed in this study, due to time-constraints, was to evaluate the systematic errors that was induced by the new reweighing method, and how it would alter with each PID selection. A more thorough study on the reweighing method itself would be advised. Furthermore, as seen in Fig. 45, there seems to be problems with the different PID cuts, as well as the detector efficiencies. Any potential issues could however not be found during the time-span of this project, but should be examined more thoroughly in further studies, although this would most likely not affect the end results seen in Fig. 49 - 51 (due to the same efficiency correction being applied to all four distributions).

7 Bibliography

References

[1] Prof. Hirokazu Tamura. http://www2.kek.jp/proffice/archives/feature/2010/images/StrangeHadronTheory2.jpg. Last visited 08/05/2017.

[2] V. Khachatryan *et al.*, "Observation of Long-Range Near-Side Angular Correlations in Proton-Proton Collisions at the LHC," *JHEP*, vol. 09, p. 091, 2010.

[3] G.Shaw and B.R.Martin, *Particle Physics*. John Wiley & Sons, Inc., 1995. Page 1.

[4] Group Serra. http://www.physik.uzh.ch/groups/serra/images/SM1.png. Last visited 08/05/2017.

[5] G. Kane, *"Modern Elementary Particle Physics: The Fundamental Particles and Forces?"*. Perseus Publishing, 1993. Page 9.

[6] G. Kane, *"Modern Elementary Particle Physics: The Fundamental Particles and Forces?"*. Perseus Publishing, 1993. Pages 105-112.

[7] N. I. of Standards and Technology. http://physics.nist.gov/cgi-bin/cuu/Value?e. Last visited 08/05/2017.

[8] W. Florkowski, *Phenomenology of Ultra-Relativistic Heavy-Ion Collisions*. World Scientific Publishing Co. Pte. Ltd., 2010. Pages 6-7.

[9] Bot, "QCD (Quantum Chromodynamics)." http://cronodon.com/Atomic/QCD.html. Last visited 08/05/2017.

[10] G.Shaw and B.R.Martin, *Particle Physics*. John Wiley & Sons, Inc., 1995. Page 158.

[11] G. Kane, *"Modern Elementary Particle Physics: The Fundamental Particles and Forces?"*. Perseus Publishing, 1993. Pages 236-240.

[12] G.Shaw and B.R.Martin, *Particle Physics*. John Wiley & Sons, Inc., 1995. Pages 164-165.

[13] G.Shaw and B.R.Martin, *Particle Physics*. John Wiley & Sons, Inc., 1995. Page 160.

[14] W. Florkowski, *Phenomenology of Ultra-Relativistic Heavy-Ion Collisions*. World Scientific Publishing Co. Pte. Ltd., 2010. Page 98.

[15] V. Khachatryan, A. Sirunyan, A. Tumasyan, W. Adam, T. Bergauer, M. Dragicevic, J. Erö, C. Fabjan, M. Friedl, R. Frühwirth, *et al.*, "Measurement of the inclusive 3-jet production differential cross section in proton–proton collisions at 7 tev and determination of the strong coupling constant in the tev range," *The European Physical Journal C*, vol. 75, no. 5, pp. 1–24, 2015.

[16] K. S. Krane, *"Introductory Nuclear Physics"*. John Wiley & Sons, Inc., 1988. Pages 721-724.

[17] CERN. http://pdg.web.cern.ch/pdg/cpep/color.html. Fig 3. Last visited 08/05/2017.

[18] G. Kane, *"Modern Elementary Particle Physics: The Fundamental Particles and Forces?"*. Perseus Publishing, 1993. Page 169.

[19] A. K. Chaudhuri, *"A Short Course on Relativistc Heavy-Ion Collisions"*. Institute of Physics Publishing, 2014.

[20] J. Rafelski, "Extreme States of Nuclear Matter - 1980," pp. 282–324, 1981. [Reprint: Eur. Phys. J.A51,no.9,115(2015)].

[21] A. Dainese, "Review on Heavy-Ion Physics," *Nuovo Cim.*, vol. 33, pp. 115–122, 2010.

[22] A. Tounsi and K. Redlich, "Strangeness enhancement and canonical suppression," 2001.

[23] A. L. I. C. E. Collaboration, "Enhanced production of multi-strange hadrons in high-multiplicity proton-proton collisions," *Nat Phys*, vol. advance online publication, Apr 2017. Letter.

[24] Peter Christiansen. Personal Correspondence.

[25] GlobalSpec. http://www.globalspec.com/reference/78469/203279/appendix-i-the-spherical-coordinate-system. Last visited 08/05/2017.

[26] W. Florkowski, *Phenomenology of Ultra-Relativistic Heavy-Ion Collisions*. World Scientific Publishing Co. Pte. Ltd., 2010. Pages 27-28.

[27] N. Bakhet, M. Yu. Khlopov, and T. Hussein, "Neural Networks Search for Charged Higgs Boson of Two Doublet Higgs Model at the Hadrons Colliders," 2015.

[28] R. Rahmat. http://slideplayer.com/slide/4760635/. Last visited 08/05/2017.

[29] E. Cuautle, R. Jimenez, I. Maldonado, A. Ortiz, G. Paic, and E. Perez, "Disentangling the soft and hard components of the pp collisions using the sphero(i)city approach," 2014.

[30] T. Sjöstrand, S. Ask, J. R. Christiansen, R. Corke, N. Desai, P. Ilten, S. Mrenna, S. Prestel, C. O. Rasmussen, and P. Z. Skands, "An Introduction to PYTHIA 8.2," *Comput. Phys. Commun.*, vol. 191, pp. 159–177, 2015.

[31] G.Shaw and B.R.Martin, *Particle Physics*. John Wiley & Sons, Inc., 1995. Page 276.

[32] CERN Brochure. http://cds.cern.ch/record/1092437/files/CERN-Brochure-2008-001-Eng.pdf. Last visited 08/05/2017.

[33] CERN. https://lhc-machine-outreach.web.cern.ch/lhc-machine-outreach/images/lhc-schematic.jpg. Last visited 08/05/2017.

[34] K. Skjerdal, "Photoproduction of ρ^0 in ultra–peripheral nuclear collisions at ALICE," *J. Phys. Conf. Ser.*, vol. 455, p. 012010, 2013.

[35] J. F. Grosse-Oetringhaus, "Measuring the Charged Particle Multiplicity with ALICE," *Indian J. Phys.*, vol. 85, pp. 93–97, 2011.

[36] J. Alme *et al.*, "The alice tpc, a large 3-dimensional tracking device with fast readout for ultra-high multiplicity events," *Nuclear Instruments and Methods in Physics Research Section A*, vol. Volume 622, Iss 1, 2010.

[37] "Upgrade of the ALICE Time Projection Chamber," Tech. Rep. CERN-LHCC-2013-020. ALICE-TDR-016, Oct 2013.

[38] ALICE Collaboration. http://aliceinfo.cern.ch/Public/en/Chapter2/Chap2_TPC.html. Last visited 08/05/2017.

[39] J. Alme, Y. Andres, H. Appelshäuser, S. Bablok, N. Bialas, R. Bolgen, U. Bonnes, R. Bramm, P. Braun-Munzinger, R. Campagnolo, P. Christiansen, A. Dobrin, C. Engster, D. Fehlker, Y. Foka, U. Frankenfeld, J. Gaardhøje, C. Garabatos, P. Glässel, C. G. Gutierrez, P. Gros, H.-A. Gustafsson, H. Helstrup, M. Hoch, M. Ivanov, R. Janik, A. Junique, A. Kalweit, R. Keidel, S. Kniege, M. Kowalski, D. Larsen, Y. Lesenechal, P. Lenoir, N. Lindegaard, C. Lippmann, M. Mager, M. Mast, A. Matyja, M. Munkejord, L. Musa, B. Nielsen, V. Nikolic, H. Oeschler, E. Olsen, A. Oskarsson, L. Osterman, M. Pikna, A. Rehman, G. Renault, R. Renfordt, S. Rossegger, D. Röhrich, K. Røed, M. Richter, G. Rueshmann, A. Rybicki, H. Sann, H.-R. Schmidt, M. Siska, B. Sitár, C. Soegaard, H.-K. Soltveit, D. Soyk, J. Stachel, H. Stelzer, E. Stenlund, R. Stock, P. Strmeň, I. Szarka, K. Ullaland, D. Vranic, R. Veenhof, J. Westergaard, J. Wiechula, and B. Windelband, "The {ALICE} tpc, a large 3-dimensional tracking device with fast readout for ultra-high multiplicity events," *Nuclear Instruments and Methods in Physics Research Section A: Accelerators, Spectrometers, Detectors and Associated Equipment*, vol. 622, no. 1, pp. 316 – 367, 2010.

[40] G.Shaw and B.R.Martin, *Particle Physics*. John Wiley & Sons, Inc., 1995. Page 57.

[41] L. Bryngemark, "Charged pion identification at high pT in ALICE using TPC dE/dx," in *6th International Workshop on High-pT physics at LHC (HPT 2011) Utrecht, The Netherlands, April 4-7, 2011*, 2011.

[42] ALICE Collaboration. http://aliceinfo.cern.ch/Public/en/Chapter2/Chap2_TOF.html. Last visited 08/05/2017.

[43] L. Bryngemark, "Charged pion identification at high pT in ALICE using TPC dE/dx," in *6th International Workshop on High-pT physics at LHC (HPT 2011) Utrecht, The Netherlands, April 4-7, 2011*, 2011.

[44] P. Cortese *et al.*, *ALICE forward detectors: FMD, TO and VO: Technical Design Report.* Technical Design Report ALICE, Geneva: CERN, 2004. Submitted on 10 Sep 2004.

[45] ALICE Collaboration. http://aliceinfo.cern.ch/Public/en/Chapter1/Events-en.html. Last visited 08/05/2017.

[46] Y. Levinsen, H. Burkhardt, and V. Talanov, "Simulation of Beam-Gas Scattering in the LHC," p. 4 p, Jul 2009.

[47] I. Antcheva *et al.*, "ROOT: A C++ framework for petabyte data storage, statistical analysis and visualization," *Comput. Phys. Commun.*, vol. 180, pp. 2499–2512, 2009.

[48] A. Collaboration. http://alice-offline.web.cern.ch/AliRoot/Manual.html. Last visited 08/05/2017.

[49] S. Agostinelli *et al.*, "GEANT4: A Simulation toolkit," *Nucl. Instrum. Meth.*, vol. A506, pp. 250–303, 2003.

[50] C. Patrignani *et al.*, "Review of Particle Physics," *Chin. Phys.*, vol. C40, no. 10, p. 100001, 2016.